Highlights

Impact of Parameterized Wind-Driven Boundary Layer Turbulence on the Development and Evolution of Submesoscale Mixed Layer Eddies in an Idealized Front

Xinghao Jiang, Qing Li

- Mixed layer eddies (MLE) are sensitive to boundary layer turbulence (BLT) schemes.
- Parameterized wind-driven BLT mostly affects MLEs before they are fully developed.
- The competing effects of MLE and BLT on stratification should be considered jointly.
- BLT affects Ekman-induced stratification by modulating submesoscale vertical shear.

Impact of Parameterized Wind-Driven Boundary Layer Turbulence on the Development and Evolution of Submesoscale Mixed Layer Eddies in an Idealized Front

Xinghao Jiang[a], Qing Li[a,b,*]

[a] *Earth, Ocean and Atmospheric Sciences Thrust, The Hong Kong University of Science and Technology (Guangzhou), Guangzhou, Guangdong, China*
[b] *Center for Ocean Research in Hong Kong and Macau, The Hong Kong University of Science and Technology, Hong Kong, China*

Abstract

Submesoscale mixed layer eddies (MLE) and boundary layer turbulence (BLT) are two predominant physical processes in the ocean surface mixed layer that overlap in spatial and temporal scales. Their interaction may strongly modulate vertical mixing in the upper ocean, but has not yet been included in ocean general circulation models (GCM), in which their effects are parameterized separately. In addition, as MLEs are progressively resolved in global ocean GCMs with increasing computational resources, BLT will likely remain unresolved and require parameterizations in the foreseeable future. It is therefore essential to quantify the impact of parameterized BLT on the development and evolution of MLEs, in particular when BLT is actively driven by surface winds. Here we compare simulated MLEs at an idealized sub-

*Corresponding author
Email addresses: xjiang578@connect.hkust-gz.edu.cn (Xinghao Jiang), ocqingli@hkust-gz.edu.cn (Qing Li)

mesoscale front with down-front wind-driven BLT parameterized by KPP and k-ε. We found that a stronger parameterized BLT-induced vertical mixing results in intensified submesoscale vertical motions, enhanced vertical buoyancy transport, and increased MLE-induced restratification rates. This close coupling between MLE-induced restratification and BLT-induced destratification can be largely attributed to the increase of available potential energy by BLT-induced vertical mixing in frontal regions, which is extracted by MLEs through mixed layer instability. This suggests that uncertainties in BLT parameterizations can lead to uncertainties in the simulated MLEs. Therefore, their impact on vertical transport of heat and materials should be assessed together. In addition, our results also suggest that parameterizations of BLT and MLE in coarse-resolution GCMs should be implemented jointly rather than separately.

Keywords:

Submesoscale Mixed Layer Eddy, Boundary Layer Turbulence, Parameterizations, Stratification

---

1. Introduction

Ocean surface boundary layer turbulence (BLT) and submesoscale mixed layer eddies (MLE) are two predominant physical processes in the ocean mixed layer. Both processes play an important role in regulating the exchange of heat, momentum, and materials between the atmosphere and ocean interior, and thus have important implications for the energy budget in the ocean (e.g., Capet et al., 2008c; McWilliams, 2016; Hypolite et al., 2023) and the marine ecosystem (e.g., Taylor and Ferrari, 2011; Mahadevan et al.,

2012; Mahadevan, 2016). The BLT is characterized by nearly isotropic turbulent flows that are minimally affected by Earth's rotation (Rossby number $\mathrm{Ro} \gg 1$), with a spatial scale of 0.1–100 m and a time scale of hours. It is primarily driven by surface forcing, such as wind, surface waves, and destabilizing surface buoyancy flux, and contributes to turbulent mixing in the upper ocean mainly in the vertical due to its small size in the horizontal, eroding stratification by converting turbulent kinetic energy (TKE) into potential energy (D'Asaro, 2014). The MLE exhibits significant anisotropy in horizontal versus vertical directions due to Earth's rotation ($\mathrm{Ro} \sim 1$), with a horizontal spatial scale of 0.1–10 km and a time scale of hours to days (McWilliams, 2016; Taylor and Thompson, 2023). It arises from the mixed layer instability (or submesoscale baroclinic instability), extracting available potential energy from the tilted isopycnals in the mixed layer (Boccaletti et al., 2007; Fox-Kemper et al., 2008). By converting potential energy into kinetic energy that energizes themselves, MLEs contribute to the restratification of the mixed layer. In this sense, BLT and MLE play a competing role in affecting the stratification of the upper ocean and the depth of the mixed layer. Indeed, when parameterized separately in large-scale ocean general circulation models (GCM) in which both processes are not resolved, assuming a scale separation (thus no interaction) between the two, the effect of MLE is primarily a shoaling of the simulated mixed layer depth (e.g., Fox-Kemper et al., 2011), opposite to the deepening effect of BLT (e.g., Li et al., 2016).

However, the interaction between BLT and MLE may not be ignored, given that they generally coexist in the upper ocean and there is significant overlap between their characteristic spatial and temporal scales. Great efforts

have been made in recent years to elucidate the mechanisms and effects of their interaction from different perspectives. For example, Callies and Ferrari (2018) found that mixed layer instability is able to persistently grow under moderate to strong convective forcing conditions and modify the convective turbulence structures, even if its restratifying effect is outcompeted by the destratifying effect of convective turbulence. The vertical buoyancy flux associated with these submesoscale MLEs can be significantly enhanced in the presence of convective turbulence (Verma et al., 2022; Aparco-Lara et al., 2023). In the presence of down-front winds, a destabilizing Ekman buoyancy flux (Thomas and Lee, 2005) enhances frontogenesis and, combined with destabilizing surface buoyancy flux, results in gravitational instability and forced symmetric instability that affect turbulent mixing and boundary layer growth (Taylor and Ferrari, 2010). In addition, Skyllingstad et al. (2017) showed that the ageostrophic shear instability, modulated by inertial oscillation, also contributes to coherent roll structures and turbulent mixing in frontal regions. The presence of surface waves further complicates the dynamics, promoting Langmuir turbulence that can either enhance or suppress frontogenesis depending on the alignment between surface waves and fronts (Hamlington et al., 2014; Suzuki et al., 2016; Sullivan and McWilliams, 2019). It is now clear that turbulent mixing by BLT is strongly modified by the presence of the horizontal buoyancy gradient induced by submesoscale features such as MLEs (e.g., Yuan and Liang, 2021). On the other hand, the life cycle of submesoscale fronts and the resulting MLEs are also affected by BLT-induced vertical momentum flux through turbulent thermal wind balance and vertical buoyancy flux that directly changes the frontal struc-

ture (e.g., McWilliams et al., 2015; Sullivan and McWilliams, 2024; Dauhajre et al., 2025). Consequently, conventional BLT-induced vertical mixing parameterizations often fail in frontal regions (Johnson and Fox-Kemper, 2024), whereas the MLE parameterization by Fox-Kemper et al. (2008) also requires modifications to account for the impact of BLT (Bodner et al., 2023).

High-resolution large eddy simulations (LES) in a sufficiently large domain that allows the development of submesoscale features have been shown to be tremendously helpful in studying the interaction between BLT and MLE (e.g., Hamlington et al., 2014; Sarkar et al., 2016; Skyllingstad et al., 2017; Sullivan and McWilliams, 2019). However, the extremely high computational cost of these LESs hinders a systematic exploration of the vast parameter space. In addition, elucidating the complex interactions between BLT and MLE in these simulations is not easy (Suzuki et al., 2016; Johnson and Fox-Kemper, 2024). An alternative approach that examines the response of simulated submesoscale MLE to parameterized BLT (e.g., Ramachandran et al., 2013; Mukherjee et al., 2016; Wang et al., 2022) also sheds light on the impact of BLT on MLE. We take this latter approach in this paper, studying the impact of parameterized BLT on MLE in terms of its flow evolution, vertical momentum and buoyancy fluxes, and the resulting stratification. Given that there are still large uncertainties in the parameterization of BLT-induced vertical mixing (Li et al., 2019), it is useful to examine the sensitivity of the simulated MLE to different choices of BLT parameterizations. This is also of practical use as submesoscale MLEs are routinely resolved in realistic regional simulations (e.g., Capet et al., 2008a; Mahadevan et al., 2012) and gradually permitted in global simulations (e.g., Rocha et al., 2016), whereas BLT will

remain unresolved (thus require parameterizations) in these simulations in a foreseeable future (Fox-Kemper et al., 2014).

We focus on the MLEs developed on a submesoscale front with uniform destabilizing down-front winds and zero surface buoyancy flux in an idealized double-front configuration (similar to the configuration in Hamlington et al., 2014), in a regime where the wind-driven currents are comparable to the MLE-induced currents (see more details in Section 2.3). In particular, we directly simulate these idealized submesoscale MLEs using an ocean GCM, MPAS-Ocean (Ringler et al., 2013), and compare their development and evolution with BLT parameterized by either the K-Profile Parameterization (KPP, Large et al., 1994) or the k-ε model (Rodi, 1987). KPP and k-ε represent two different classes of BLT parameterizations that are widely used in the ocean modeling community and, to some extent, represent the remaining uncertainty in parameterizing the BLT-induced vertical mixing (Li et al., 2019). While the sensitivity of simulated submesoscale flows to the choice of BLT parameterizations has been discussed in previous studies (e.g., Ramachandran et al., 2013; Mukherjee et al., 2016; Wang et al., 2022), here we focus on a different dynamic regime. Our double-front configuration with uniform down-front wind stress differs from the single-front configuration with cross-frontally varying wind stress in Ramachandran et al. (2013) and Mukherjee et al. (2016). This allows us to avoid the unnecessary Ekman pumping associated with spatially varying wind stress, which obscures the impact of parameterized BLT-induced vertical mixing on the evolution of MLEs. It also differs from the submesoscale MLEs generated at an idealized mesoscale eddy with no surface wind forcing in Wang et al. (2022), in which

the surface-forced BLT is not activated.

The goals of this study are to clarify the following three questions. (1) Are the development and evolution of submesoscale MLEs sensitive to the BLT parameterization? (2) How does the BLT parameterization affect the MLE-induced vertical momentum and buoyancy fluxes? (3) How is MLE-induced restratification modified by different parameterized destratification rates due to BLT?

The remainder of this paper is organized as follows. Section 2 describes the GCM and BLT parameterizations used in this study, as well as the experimental setup. Section 3 examines the impact of different BLT parameterizations on the evolution of MLEs at different stages. Section 4 discusses the different BLT-induced vertical mixing given by these parameterizations. The impact of different BLT parameterizations on MLEs is further analyzed in Section 5 from the perspective of modulating the vertical shear, vertical fluxes, and restratification rates. Finally, we summarize our main findings in Section 6.

2. Methods

2.1. MPAS-Ocean

In this study, the Model for Prediction Across Scales-Ocean (MPAS-Ocean, Ringler et al., 2013) is used to simulate MLEs on idealized submesoscale fronts. MPAS-Ocean solves the hydrostatic and incompressible primitive equations with the Boussinesq approximation on an unstructured mesh. It employs the finite-volume discretization using a C-grid staggering in the horizontal, z^* vertical coordinate, a split-explicit time stepping method,

and a quasi 3rd-order monotone advection scheme for tracers. More details on the numerics can be found in Ringler et al. (2010) and Ringler et al. (2013).

MPAS-Ocean is the ocean component of the Energy Exascale Earth System Model (Golaz et al., 2019). It includes various parameterizations of unresolved physics that can be individually enabled or disabled for realistic global ocean simulations at different resolution. It can also be configured on idealized domains for process studies (e.g., Li and Van Roekel, 2021). Since submesoscale features are resolved in our idealized simulations, horizontal mixing due to unresolved physics is disabled. Here, we focus on varying the parameterization of BLT-induced vertical mixing. Modifications to the code are based on MPAS-Ocean version 7.0. The modified source code and the namelist for setting up the experiments in this study are archived in Jiang and Li (2026).

2.2. Boundary Layer Turbulence Parameterizations

In the absence of surface buoyancy loss, the vertical mixing of a scalar tracer λ in the surface boundary layer is parameterized using a down-gradient model,

$$\overline{w'\lambda'} = -K_\lambda \partial_z \overline{\lambda}, \tag{1}$$

where λ can represent either a component of horizontal velocity $\mathbf{u}_h = [u, v]$ or a tracer such as temperature T or salinity S, or, for simplicity in our idealized simulations, the buoyancy b which is a function of T and S. The overline $\overline{(\cdot)}$ denotes the mean quantity over a grid cell and a time step of MPAS-Ocean (i.e., the resolved quantity), and the prime $(\cdot)'$ denotes the

turbulent fluctuations that are at the sub-grid scale. The proportionality coefficient K_λ represents the turbulent viscosity ν_t or turbulent diffusivity κ_t, which are parameterized. Since all analyses in this study are based on resolved fields in MPAS-Ocean, hereafter we drop the overline symbol for the resolved quantity for clarity except when it is used in tandem with the prime symbol to denote the sub-grid scale fluxes due to BLT.

2.2.1. KPP

KPP (Large et al., 1994) is the default parameterization scheme for BLT-induced vertical mixing in MPAS-Ocean, implemented through the Community Ocean Vertical Mixing (CVMix, Griffies et al., 2015) package. Full descriptions of the KPP formulation can be found in Large et al. (1994) and Van Roekel et al. (2018). Also, see Appendix A1 of Li et al. (2019) for a summary of some recent updates to incorporate the effects of Langmuir turbulence. We therefore exclude a detailed description of KPP here for brevity. The essence of KPP is to assume a universal profile shape ($G(\sigma) = \sigma(1-\sigma)^2$, with $\sigma = |z|/h_b$) for the turbulent viscosity ν_t in the boundary layer,

$$\nu_t = h_b w_s(\sigma) G(\sigma), \tag{2}$$

scaled by the boundary layer depth h_b and a velocity scale w_s that depends on the surface forcing and varies with σ according to the Monin-Obukhov similarity theory. The turbulent diffusivity κ_t is parameterized in a similar way with a different Monin-Obukhov similarity function. Here, we use default values for the free parameters in KPP as recommended in CVMix. Note that the modification of KPP by Thomas (2005) to account for the effects of Ekman buoyancy flux is not included.

To further investigate the sensitivity of the simulated MLE to the strength of BLT-induced vertical mixing, an augmented KPP (denoted hereafter as A-KPP) with ν_t and κ_t multiplied by a factor of $\mathcal{E} = 1.2$ is also tested. This is motivated by a common practice to account for the enhanced vertical mixing due to Langmuir turbulence by applying an enhancement factor to the turbulent velocity scale (McWilliams and Sullivan, 2000; Li et al., 2019). An enhancement factor of $\mathcal{E} = 1.2$ corresponds to its peak value in the broader distribution (between $\sim$ 0.8 and $\sim$ 1.8) that represents typical conditions in the global ocean (see Fig. A1 in Li et al., 2019). We also tested different values of $\mathcal{E}$. With sufficiently large values (e.g., $\mathcal{E} = 2.0$), the BLT-induced destratification dominates over the MLE-induced restratification, while MLEs persistently grow and evolve, consistent with Callies and Ferrari (2018).

2.2.2. k-ε

Additional options for parameterizing BLT-induced vertical mixing are implemented in MPAS-Ocean through the General Ocean Turbulence Model (GOTM, Umlauf and Burchard, 2005). Specifically, we use the generic length-scale scheme (Umlauf and Burchard, 2003) in the k-ε formulation (Rodi, 1987). The k-ε model parameterizes the turbulent viscosity ν_t by

$$\nu_t = c_\mu \frac{k^2}{\varepsilon}, \tag{3}$$

where k is the turbulent kinetic energy (TKE), ε is the dissipation rate of TKE, and c_μ is a dimensionless stability function that can be obtained by solving the simplified Reynolds stress equations in equilibrium (or quasi-equilibrium) state (see more discussions in Umlauf and Burchard, 2005).

Here we use the weak-equilibrium stability function with coefficients given by Canuto et al. (2001). The turbulent diffusivity κ_t can be parameterized similarly using a different stability function obtained by solving the simplified turbulent buoyancy flux equation.

The k-ε model evolves prognostic equations for k and ε. It therefore has memory of previous turbulence states, in contrast to KPP which only depends on the instantaneous forcing and background states by assuming that the BLT evolves into an equilibrium state quickly. In addition, by using stratification $N^2 = \partial_z b$ and velocity shear squared $S^2 = (\partial_z u)^2 + (\partial_z v)^2$ at each vertical level as inputs, it also directly captures the transition between the boundary layer and the interior with sufficiently high vertical resolution. In contrast, KPP uses a bulk Richardson number to define the boundary layer and parameterizes vertical mixing in the boundary layer and interior differently.

2.3. Model Setup

The simulation is initialized with an idealized double-front configuration in the mixed layer (as shown in Fig. 1), following the configurations in Hamlington et al. (2014) and Li and Van Roekel (2021). This contrasts with similar previous research in which a single-front configuration was adopted (e.g., Ramachandran et al., 2013; Mukherjee et al., 2016). The rationale for using the double-front configuration is to avoid the impermeable wall boundary conditions at lateral boundaries in the single-front configuration, which, in conjunction with surface wind stress, leads to Ekman pumping that affects the evolution of MLEs. Similar double-front configurations were also used in other studies, especially when surface forcing is considered (e.g., Verma

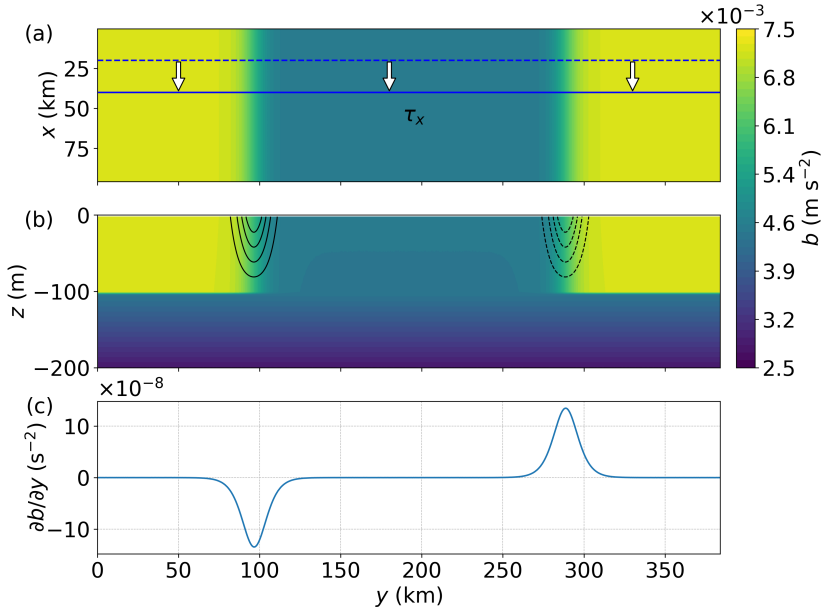

Figure 1: Initial conditions for the double-front configuration. (a) Horizontal distribution of the buoyancy b at the surface (color shading) with uniform along-front wind stress $\tau_x = 0.1$ N m^{-2} (white arrows). (b) Vertical distribution of the buoyancy (color shading, uniform in x-direction) and the along-front jets in a thermal wind balance with the horizontal buoyancy gradient assuming zero flow at the base of the mixed layer (contours with interval of 0.034 m s^{-1}, solid and dashed lines for positive and negative values, respectively). (c) Horizontal buoyancy gradient in the mixed layer.

et al., 2022; Sullivan and McWilliams, 2024).

As shown in Fig. 1, the double-front structure in the initial buoyancy field

is expressed as

$$b_0(x,y,z) = b_b + N^2(z+H) + \frac{L_f M^2}{2}\left[2 - \tanh\frac{2(y-y_1)}{L_f} + \tanh\frac{2(y-y_2)}{L_f}\right], \tag{4}$$

$$N^2 = \begin{cases} N^2_{\rm ml}, \text{ if } z > -H, \\ N^2_{\rm int}, \text{ if } z \le -H, \end{cases} \tag{5}$$

$$M^2 = \begin{cases} M^2_f, \text{ if } z > -H, \\ 0, \text{ if } z \le -H, \end{cases} \tag{6}$$

where $b_b = 4.5 \times 10^{-3}$ is the buoyancy at the base of the mixed layer, $H = 100$ m is the initial mixed layer depth, $N^2_{\rm ml} = 1.68 \times 10^{-7}$ s^{-2} and $N^2_{\rm int} = 1.68 \times 10^{-5}$ s^{-2} are the stratification within and below the mixed layer. The front width is $L_f = 20$ km, with the horizontal buoyancy gradient $M^2_f = 1.35 \times 10^{-7}$ s^{-2}. The initial front locations are $y_1 = 0.25L_y$ and $y_2 = 0.75L_y$, where L_y is the domain size in the cross-front direction. Small random perturbations (2×10^{-7} m s^{-2}) are added to the initial buoyancy field to promote the development of MLEs. The Coriolis parameter is $f = 7.7 \times 10^{-5}$ s^{-1}, corresponding to an inertial period $T_f = 22.67$ h. The two fronts are initialized from along-front jets that are in thermal wind balance with the horizontal buoyancy gradients, with zero flow at the base of the mixed layer.

Since we are interested in the impact of wind-driven BLT on the evolution of MLE, the surface is forced by a uniform along-front wind stress of $\tau_x = 0.1$ N m^{-2}. The choice of the wind stress magnitude is guided by a scaling parameter measuring the relative importance of the wind forcing and MLE

(Mahadevan et al., 2010),

$$r = \left| \frac{\psi_{\text{wind}}}{\psi_{\text{mle}}} \right|, \tag{7}$$

where $\psi_{\text{wind}} \sim -\tau_x/\rho_0 f$ (with $\rho_0 = 1025.6$ kg m^{-3} the seawater density) measures the strength of the overturning stream function by Ekman transport, and $\psi_{\text{mle}} \sim 0.06 H^2 M_f^2 / f$ measures the strength of the overturning stream function due to MLE (Fox-Kemper et al., 2008). The combination of parameters in this configuration results in $r \approx 1.20$, suggesting comparable wind forcing and MLE.

The computational domain is $L_x \times L_y \times L_z = 96$ km $\times$ 384 km $\times$ 500 m in the along-front (L_x), cross-front (L_y) and vertical (L_z) directions, using uniform hexagon cells in the horizontal and fixed vertical levels with surface refinement. The horizontal grid spacing is 500 m. The vertical resolution is 2 m near the surface and gradually coarsens to 10 m near the bottom. The wavelength of the fastest growing mode of the mixed layer baroclinic instability (Stone, 1966, 1970) is given by

$$L_{\text{MLI}} = \frac{2\pi U}{|f|} \sqrt{\frac{1 + \text{Ri}}{5/2}}, \tag{8}$$

where U is the mean shear velocity scale and Ri is the Richardson number. Using typical values of $U = 0.1$ m s^{-1} and Ri $= 0.5$ in the mixed layer in our simulations, $L_{\text{MLI}} \approx 6$ km. A horizontal grid spacing of 500 m is sufficient to resolve this fastest growing mode. We also performed sensitivity tests by varying the horizontal grid spacing between 300 m and 600 m and found little changes in the results. Note that this computational domain is significantly larger than previous studies in both the along-front and cross-front directions, so that a sufficiently large number of MLEs could develop on

the front for robust along-front statistics, and the two fronts are sufficiently separated from each other throughout the simulations.

This double-front problem is solved using the three BLT parameterizations described in the previous section (specifically, KPP, A-KPP, and k-ε). Although a relatively large along-front domain size L_x is used here, significant variations in the along-front MLE statistics were found during analyses of the initial results, primarily due to the evolution of individual MLEs. Therefore, eight ensemble simulations were conducted for each BLT parameterization, with different random perturbations (by varying the random seeds) on the initial buoyancy field to enhance the robustness of the statistical analysis. The ensemble spread across eight ensemble members provides an estimate of the uncertainty of the MLE statistics. Comparison of snapshots with different BLT parameterizations is done using the first ensemble member with the same initial random perturbation. Other ensemble members show similar results. All simulations are run for 20 days (21.2 inertial periods) with a time step of 2 minutes. The output are saved every 3 hours for analysis.

Due to Earth's rotation, the along-front wind generates an Ekman transport to the right of the wind. This results in an unstable front where denser water is transported over lighter water, and a stable front where lighter water is transported over denser water. Submesoscale MLEs form on the unstable front, which is the focus here. To assist in the analysis of MLE-induced transport, we define an along-front average $\widetilde{(\cdot)}$ of a quantity q as

$$\widetilde{q} = \frac{1}{L_x} \int_0^{L_x} q \, dx, \tag{9}$$

so that the fluctuations on top of this mean,

$$q^{\dagger} = q - \widetilde{q}, \tag{10}$$

represent variations due to MLEs. Note that this decomposition into the along-front average and fluctuations is performed in each ensemble member, and the mean and spread of the ensemble are computed subsequently.

As the submesoscale front is continuously evolving and moving with Ekman transport, we define a frontal region R_f using the instantaneous along-front averaged horizontal kinetic energy $\widetilde{|\mathbf{u}_h|^2}/2$ at 10 m depth to assist in the quantitative analysis of MLE statistics in the following sections. Using $\widetilde{|\mathbf{u}_h|^2}/2$ at a different depth in the mixed layer yields similar results. The background kinetic energy is first estimated from regions sufficiently far from the front, and then R_f is identified as the region where the kinetic energy exceeds this background value by 10^{-3} m^2 s^{-2}. Using this definition on the unstable front, R_f gradually widens as MLEs develop on the front. We further restrict the analysis of MLE statistics within the mixed layer, whose depth h_m is defined as the depth at which the density varies from its surface value by 0.03 kg m^{-3} (de Boyer Montégut et al., 2004). These definitions identify a region where both MLE and BLT are actively occurring. Therefore, a horizontal frontal average $\langle\cdot\rangle_h$ of the quantity q is defined as

$$\langle q\rangle_h = \frac{1}{A}\iint_{R_f} q\, dA, \tag{11}$$

$$A = \iint_{R_f} dA, \tag{12}$$

where dA is a horizontal area element. And a three-dimensional (3D) frontal

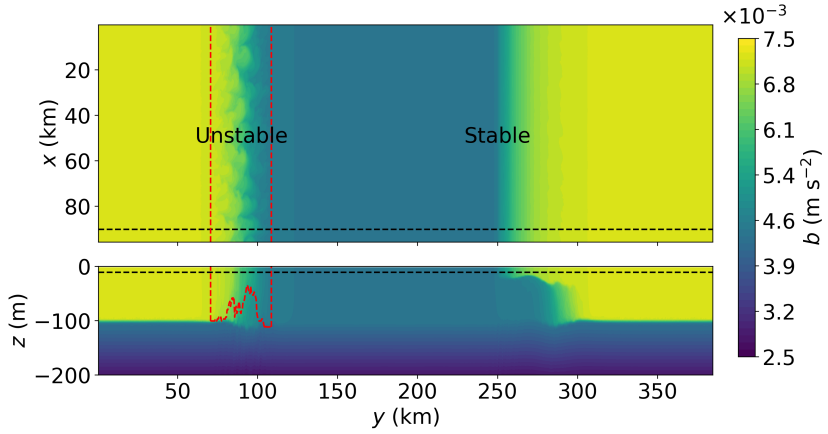

Figure 2: Horizontal (top panel) and vertical (bottom panel) distribution of the buoyancy b in the KPP case, when MLEs are at an early stage of development ($t = 6.4T_f$). Black dashed lines mark the locations of the horizontal and vertical slices. Red dashed lines denote the boundaries of the unstable frontal region in the horizontal and vertical slices, defined using an eddy kinetic energy criterion and constrained within the mixed layer (see Section 2.3 for more details).

average $\langle\cdot\rangle$ is defined by first taking an average over the mixed layer,

$$\langle q \rangle = \left\langle \frac{1}{h_m} \int_{-h_m}^{0} q \, dz \right\rangle_h . \tag{13}$$

An example is provided in Fig. 2, in which the frontal region is enclosed by the dashed lines in red. Given the dependence of (13) on the mixed layer depth h_m, whose definition can be ambiguous (e.g., Reichl et al., 2022), we also tested an alternative 3D frontal average by using the initial mixed layer depth $h_m = H$, which yielded qualitatively similar results.

3. Evolution of Flow Structures

We first examine the effect of different BLT parameterizations on the evolution of flow structures in MLEs. Fig. 3 shows snapshots of the vertical

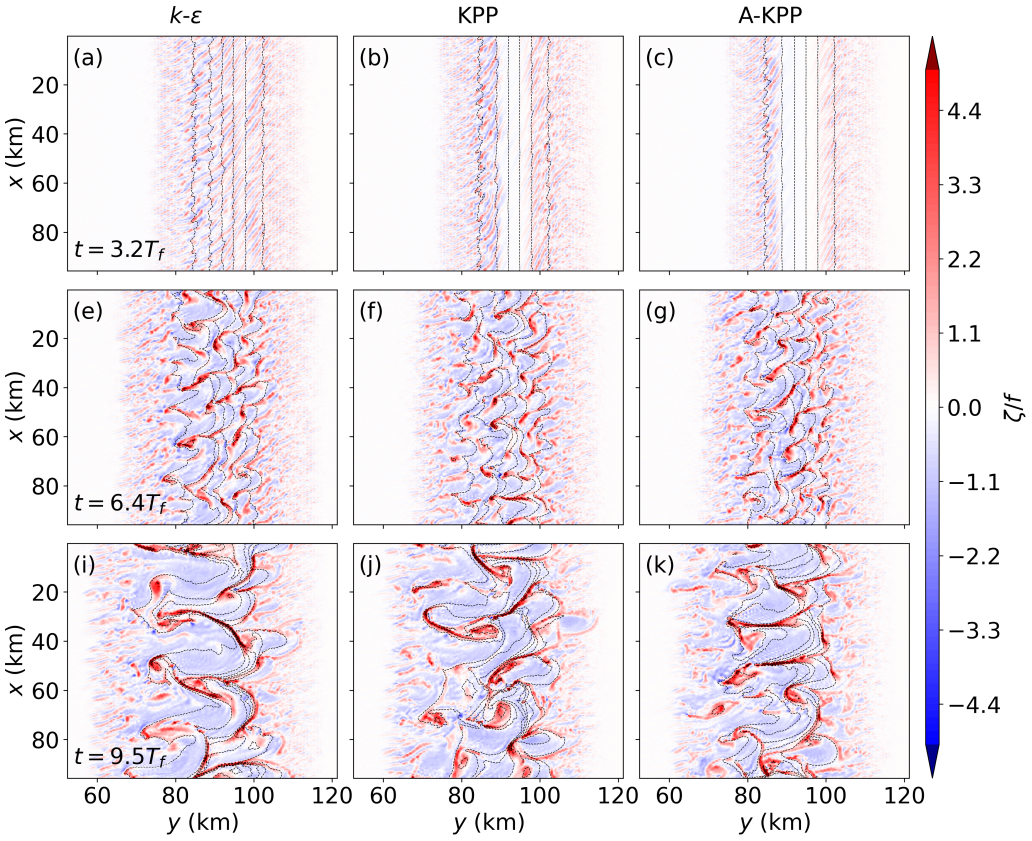

Figure 3: Snapshots of normalized relative vorticity in three time instances ($t = [3.2, 6.4, 9.5]T_f$) showing the evolution of submesoscale MLEs with different BLT parameterizations. Color shading shows the relative vorticity ($\zeta = \partial_x v - \partial_y u$) normalized by the Coriolis parameter f. Overlaid dashed lines show isopycnals with interval of 0.04 kg m^{-3}.

component of the relative vorticity ($\zeta = \partial_x v - \partial_y u$) normalized by the Coriolis parameter f in three time instances. In general, the three BLT parameterizations result in a consistent evolution of MLEs. In all three cases, wave-like structures appear around $3T_f$ and then rapidly develop into submesoscale MLEs, reaching a size of ~ 20 km after $9T_f$.

Closer inspection shows slightly different flow structures in the early stage of the MLE evolution (top panels in Fig. 3). The KPP case shows a very small magnitude of vertical vorticity in the center of the front but remarkable wave-like flow structures at both sides. These wave-like structures at two sides of the front gradually develop and extend to the center of the front. Increased turbulent viscosity and diffusivity in the A-KPP case results in a smaller magnitude of vertical vorticity at two sides of the front than in the KPP case. But similar to the KPP case, vertical vorticity at the center of the front is very weak, indicating that the frontal jet has not been significantly influenced by mixed layer instability in this stage. In contrast, the k-ε case shows active wave-like structures of strong vertical vorticity across the frontal regions. This suggests that both the magnitude and the distribution of turbulent viscosity (and diffusivity) impact the response of submesoscale frontal jet to mixed layer instability in the early stage of the frontal evolution when the mixed layer instability initiates. Note that these differences among the three cases in the evolution of vertical vorticity depend on the background flow (i.e., M_f^2), suggesting a competition between mixed layer instability that generates wave-like structures and boundary layer turbulence that tends to homogenize the flow. However, the differences among the three cases are much more difficult to discern in the later stages when MLEs are fully developed. As a

result, the resulting turbulence statistics are also similar in the later stages, as will be shown next.

To quantify the impact of BLT parameterizations on MLE evolution, Fig. 4 shows the time series of the frontal averaged and normalized stratification, mixed layer depth, horizontal kinetic energy, vertical vorticity, lateral buoyancy variation, and the frontogenesis rate. Following Capet et al. (2008b), the horizontal strain-induced frontogenesis rate F_s is defined as

$$F_s = \mathbf{Q} \cdot \nabla_h b, \tag{14}$$

where

$$\mathbf{Q} = -(\partial_x u \partial_x b + \partial_x v \partial_y b, \partial_y u \partial_x b + \partial_y v \partial_y b). \tag{15}$$

As shown in these plots, the evolution of MLEs can be divided into two stages. During the early stage of MLE growth (approximately from $t = 5T_f$ to $t = 10T_f$), the mixed layer instability extracts potential energy from the front and converts it into kinetic energy. As a result, the stratification (Fig. 4a) of the frontal region continues to increase as the mixed layer depth shoals (Fig. 4b), consistent with the trend of kinetic energy in Fig. 4c. This conversion from potential energy to kinetic energy is also strongly modulated by the inertial oscillation. Approximately after $t = 10T_f$, both the kinetic energy and the stratification plateau. This indicates that the MLEs are fully developed in this later stage. The MLE-induced restratification and the BLT-induced destratification are roughly in balance with each other, and thus the stratification stabilizes.

With the evolution of MLEs, all MLE statistics in Fig. 4 exhibit progressively greater sensitivity to initial random perturbations. This is due to

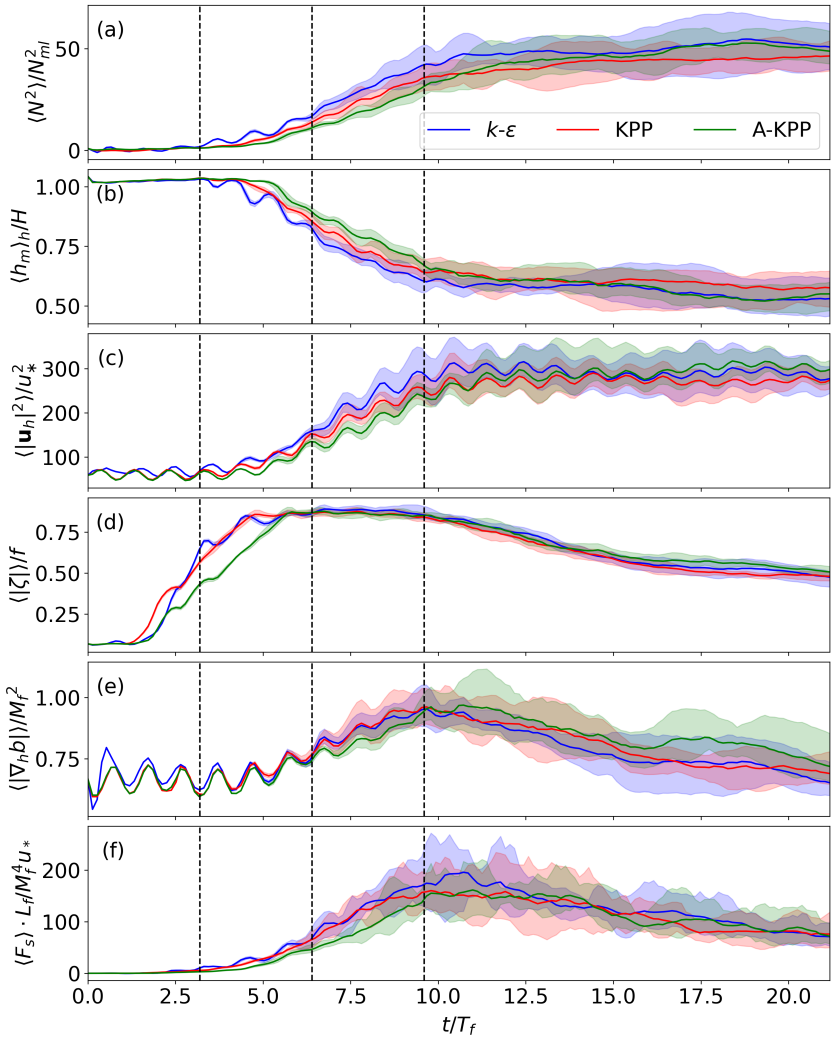

Figure 4: Time evolution of the frontal averaged (a) stratification $\langle N^2\rangle$ normalized by the initial stratification in the mixed layer N^2_{ml}, (b) mixed layer depth $\langle h_m\rangle_h$ defined by a density criterion (see Section 2.3) and normalized by the initial mixed layer depth H, (c) horizontal kinetic energy $\langle|\mathbf{u}_h|^2/2\rangle$ normalized by the friction velocity $u_* = \sqrt{\tau_x/\rho_0}$, (d) magnitude of the relative vorticity $\langle|\zeta|\rangle$ normalized by the Coriolis parameter f, (e) horizontal buoyancy gradient $\langle|\nabla_h b|\rangle = \langle\sqrt{(\partial_x b)^2 + (\partial_y b)^2}\rangle$ normalized by the initial characteristic horizontal buoyancy gradient M_f^2, and (f) frontogenesis rate due to horizontal strain $\langle F_s\rangle$ normalized by $M_f^4 u_*/L_f$. Colored shading represents the fluctuation range among the eight ensemble members. Black dashed lines denote the three time instances in Fig. 3.

the impact of individual MLEs. As they grow bigger in size, fewer number of MLEs is allowed in the limited domain, so that the MLE statistics are increasingly skewed by the specific evolution of individual MLEs and reflect less of an averaged state. Nevertheless, the ensemble averaged MLE statistics (which are less prone to variations due to individual MLEs) show some interesting differences among cases with different BLT parameterizations.

During the first stage of the evolution of MLEs, the k-ε case shows the fastest increase in kinetic energy, compared to the KPP and A-KPP cases (Fig. 4c). A large part of this increase can be attributed to the development of submesoscale vorticity (Fig. 4d). The rapid increase in kinetic energy may be related to the increase in the frontogenesis rate and horizontal buoyancy variation, which provide the available potential energy for the development of mixed layer instability. As shown in Fig. 4e, f, the k-ε case exhibits a slightly higher horizontal buoyancy gradient than the A-KPP case and also a higher frontogenesis rate than both KPP and A-KPP cases. The enhanced turbulent viscosity and diffusivity in the A-KPP case results in slightly slower increase of kinetic energy and stratification compared to the KPP case, as the horizontal buoyancy gradient and frontogenesis rate in the A-KPP case are also smaller (Fig. 4e, f). The resulting difference in the submesoscale vorticity is more prominent (Fig. 4d). Although Sullivan and McWilliams (2024) showed that BLT-induced vertical momentum mixing promotes frontogenesis and causes convergence of horizontal flow by initiating submesoscale secondary circulation, the ensemble averaged results in Fig. 4 suggest that the enhanced turbulent viscosity and diffusivity (as in the A-KPP case) can also suppress submesoscale frontogenesis. According to Dauhajre et al. (2025), BLT plays

a dual role in submesoscale frontogenesis: the BLT-induced vertical mixing of momentum favors frontogenesis, whereas the BLT-induced vertical mixing of buoyancy promotes frontolysis. This complex role of BLT-induced vertical mixing may contribute to the fluctuations between ensemble members in both the horizontal buoyancy variation and the frontogenesis rate, which are similar in magnitude in all three cases.

During the second stage, both the frontogenesis rate and the horizontal buoyancy variation continue to decrease and gradually converge to a constant value. This stage follows the arrest of frontogenesis. During this period, the k-ε case exhibits higher kinetic energy and stratification and shallower mixed layer depth, but a similar horizontal buoyancy gradient and frontogenesis rate compared to the KPP case. The A-KPP case shows nearly the same kinetic energy and stratification as the k-ε case, but a larger horizontal buoyancy gradient than both the KPP and k-ε cases. This indicates that both the magnitude and distribution of the parameterized viscosity and diffusivity due to BLT affect the evolution of MLEs. However, the fluctuation ranges of the MLE statistics in Fig. 4 in the second stage overlap between different cases, indicating that the influence of BLT on the evolution of these MLE statistics is rather limited. It should be noted that, except for the stratification and mixed layer depth, all the MLE statistics discussed here depend on the horizontal velocity and its gradients. Since MLEs are fully developed in this stage, having a maximum size of approximately 20 km, the differences in the parameterized BLT-induced vertical mixing may not be large enough to cause significant differences in the resolved submesoscale horizontal velocity and its gradients. This also suggests that the evolution of these MLE statistics is

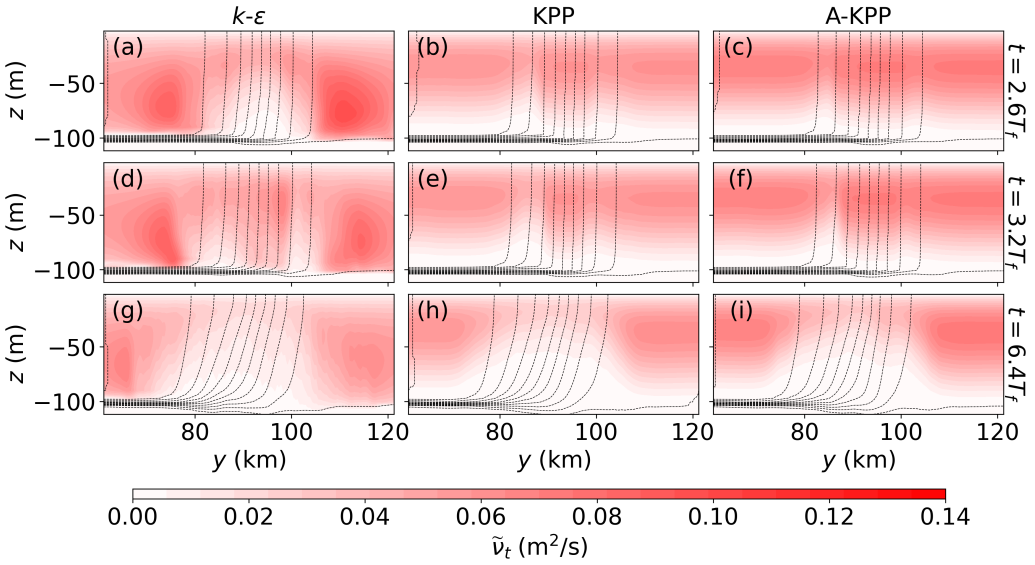

Figure 5: Parameterized turbulent viscosity averaged in the along-front direction in three arbitrarily chosen time instances before ($t = [2.6, 3.2]T_f$) and after ($t = 6.4T_f$) the emergence of MLEs. Black dashed lines represent isopycnals with an interval of 0.021 kg m^{-3}.

robust to BLT parameterizations when the MLEs are fully developed.

4. BLT-Induced Vertical Mixing

Before investigating in more detail the impact of BLT-induced vertical mixing on MLEs, it is helpful to examine the parameterized turbulent viscosity and the resulting BLT-induced turbulent fluxes in the presence of evolving MLEs. Fig. 5 shows the along-front averaged turbulent viscosity parameterized by the three BLT parameterizations. Before the emergence of MLEs ($t = 2.6T_f$ and $t = 3.2T_f$), the KPP and A-KPP cases show a nearly horizontally homogeneous turbulent viscosity across the front, whereas the k-ε case displays a larger spatial heterogeneity across the front and varia-

tions in time at the center of the front due to inertial oscillations (Fig. 5a,d). The turbulent viscosity patterns in the KPP and A-KPP cases are determined by the shape function $G(\sigma)$. As expected, the magnitude of turbulent viscosity in the A-KPP case (with a maximum value of 0.072 $\mathrm{m^2\ s^{-1}}$ at $t = 3.2T_f$) is nearly 1.2 times that of the KPP case (with a maximum value of 0.060 $\mathrm{m^2\ s^{-1}}$ at $t = 3.2T_f$). The distribution of turbulent viscosity in the k-ε case is governed by prognostic equations of the TKE and its dissipation rate, which are nonlinear and closely related to the state of the submesoscale flow. The fluctuations in the turbulent viscosity therefore arise from the flow adjustment from the initial thermal wind balance to a turbulent thermal wind balance (see more details in Section 5.1). After the emergence of MLEs ($t = 6.4T_f$), the turbulent viscosity is significantly suppressed and confined to a much thinner boundary layer (with a minimum depth of around 20 m) in all three cases. The suppression of BLT-induced turbulent viscosity in frontal regions by the presence of MLEs aligns with the results of turbulence resolving LES on large horizontal domains presented in Johnson and Fox-Kemper (2024). Interestingly, outside the front, k-ε predicts higher turbulent viscosity than KPP and A-KPP prior to the development of MLEs (Fig. 5a–c), but lower turbulent viscosity in later stages (Fig. 5g–i). This is likely a result of its higher sensitivity to the evolving stratification by solving prognostic equations of k and ε, in contrast to KPP which depends only on the bulk properties (e.g., the bulk Richardson number).

The resulting evolutions of frontal averaged and normalized BLT-induced turbulent fluxes of horizontal momentum ($\langle\overline{w'u'}\rangle$ and $\langle\overline{w'v'}\rangle$) and buoyancy ($\langle\overline{w'b'}\rangle$) are shown in Fig. 6. After MLEs emerge, the magnitude of along-

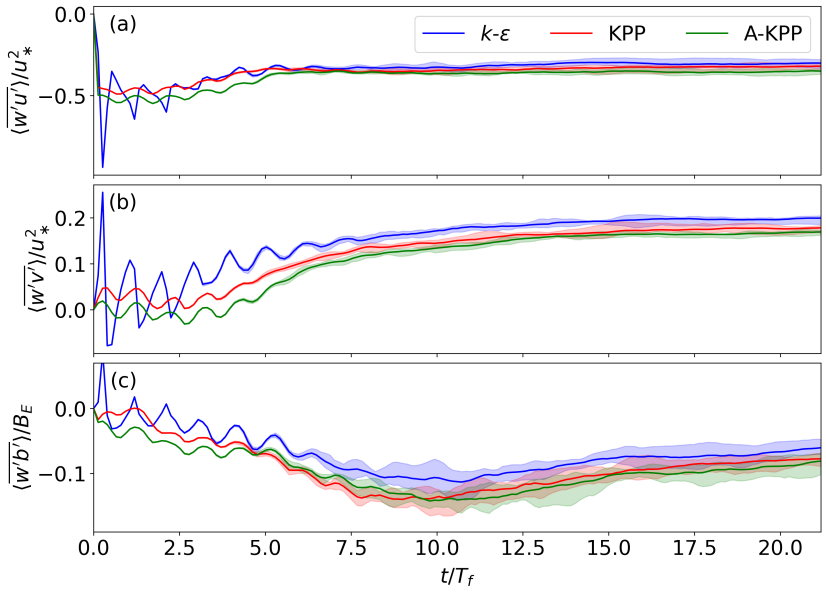

Figure 6: Time evolution of the parameterized BLT-induced turbulent fluxes averaged over the frontal region and normalized by the surface friction velocity u_* and initial Ekman buoyancy flux $B_E = \tau_x M_f^2/\rho_0 f$. Colored shading represents the fluctuation range among eight ensemble members.

front turbulent momentum flux $\langle\overline{w'u'}\rangle$ follows the order A-KPP > KPP > k-ε, consistent with the ordering of the viscosity shown in Fig. 5. However, for the cross-front momentum flux $\langle\overline{w'v'}\rangle$, it exhibits an ordering of k-ε > KPP > A-KPP. The BLT-induced turbulent fluxes are governed by both submesoscale vertical shear and turbulent viscosity as they are parameterized as the product of the two using the down-gradient assumption in Eq. (1). So, the different ordering for along-front and cross-front momentum fluxes is likely because the geostrophic shear is strong in the along-front direction, but not in the cross-front direction. The turbulent buoyancy flux $\langle\overline{w'b'}\rangle$ shows a slightly complex trend among the three cases. In the first stage ($t = 5T_f$ to $t = 10T_f$), the turbulent buoyancy flux exhibits the order KPP > A-KPP > k-ε. But in the second stage (after $t = 10T_f$), this ordering changes to A-KPP > KPP > k-ε.

As enhanced turbulent viscosity and diffusivity lead to a weakening of submesoscale vertical shear, the parameterized turbulent fluxes, which represent the strength of BLT-induced vertical mixing, are less sensitive to variations in the magnitudes of turbulent viscosity and diffusivity (as reflected by the difference between KPP and A-KPP) when MLEs show up. However, the parameterized turbulent fluxes between the KPP and k-ε cases exhibit greater differences due to differences in the detailed vertical structures of the parameterized turbulent viscosity and diffusivity. This leads to larger differences in the detailed spatial distribution and time evolution in the BLT-induced turbulent fluxes between different BLT parameterizations, even though their along-front averages are similar. In the next section, we analyze how this distinct performance of the parameterized BLT modifies submesoscale MLEs

in terms of the resulting vertical shear, vertical transports, and stratification.

5. Impact of Parameterized BLT

5.1. Vertical Shear of the Horizontal Velocity

The vertical shear of the horizontal velocity at a front is described by the thermal wind balance. In the presence of significant BLT-induced turbulent mixing, a modified balance known as the turbulent thermal wind (TTW) balance is reached (McWilliams et al., 2015),

$$\partial_z u = -\frac{1}{f}\partial_y b \underbrace{-\frac{1}{f}\partial_z^2 \overline{w'v'}}_{\partial_z u_{\mathrm{blt}}}, \tag{16}$$

$$\partial_z v = \frac{1}{f}\partial_x b \underbrace{+\frac{1}{f}\partial_z^2 \overline{w'u'}}_{\partial_z v_{\mathrm{blt}}}, \tag{17}$$

where the contributions of BLT to the velocity shear are denoted as $\partial_z u_{\mathrm{blt}}$ and $\partial_z v_{\mathrm{blt}}$. Since the flow is statistically homogeneous in the along-front direction, the along-front buoyancy gradient $\partial_x b$ remains weak and the associated geostrophic velocity shear is much smaller than the BLT-induced shear term $\partial_z v_{\mathrm{blt}}$. In contrast, the cross-front buoyancy gradient $\partial_y b$, which is initially set by the frontal buoyancy gradient M_f^2, induces a geostrophic velocity shear that is comparable in magnitude to the BLT contribution $\partial_z u_{\mathrm{blt}}$.

Fig.7 shows the total vertical shear of the submesoscale flow averaged over the frontal region ($\langle \partial_z u \rangle_h$ and $\langle \partial_z v \rangle_h$, solid lines) and the portion of vertical shear induced by BLT ($\langle \partial_z u_{\mathrm{blt}} \rangle_h$ and $\langle \partial_z v_{\mathrm{blt}} \rangle_h$, dashed lines). Three time instances ($t = 6.4T_f$, $t = 10.6T_f$, and $t = 14.8T_f$) are selected, corresponding, respectively, to the active restratification by MLEs, the onset of

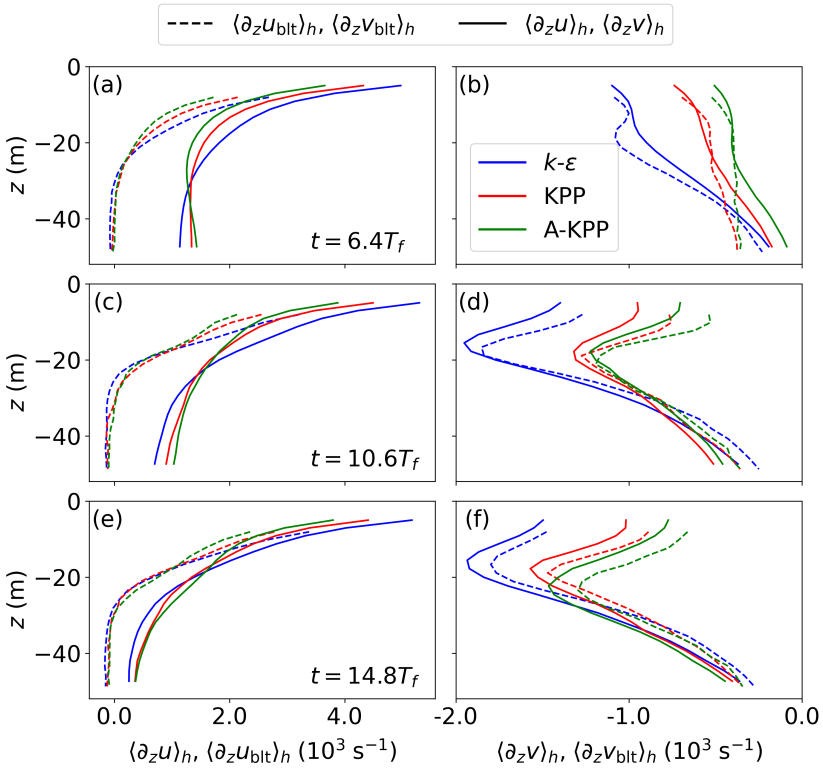

Figure 7: Vertical profiles of the total submesoscale vertical shear (solid lines) and the BLT-induced vertical shear (dashed lines) in Eq. (16) and (17) in three time instances ($t = [6.4, 10.6, 14.8]T_f$).

stable stratification, and the establishment of stable stratification. The BLT-induced vertical shear dominates the total shear throughout the evolution of MLEs, especially near the surface and after the MLEs are fully developed. In particular, the differences in the BLT portion with different BLT parameterizations dominate the differences in total shear. This suggests that the frontal averaged buoyancy gradient and the horizontal advection due to the evolution of the MLEs themselves are less affected by the choice of BLT parameterizations. This is consistent with the weak sensitivity of the mean MLE statistics to the choice of BLT parameterizations in Section 3.

Closer inspection of Fig. 7 shows that the magnitude of the total vertical shear near the surface (solid lines) can be ordered as k-ε > KPP > A-KPP, for both along-front and cross-front directions. This ordering is opposite to that of the parameterized turbulent viscosity as discussed in Section 2.2. Although the BLT-induced turbulent momentum flux is less sensitive to the choice of BLT parameterizations due to the compensation between the turbulent viscosity and vertical shear, the resulting differences in the vertical shear (in particular the cross-front shear) have substantial consequences on the evolution of stratification. The diverse vertical shear in the cross-front direction as shown in Fig.7b,d,f is attributed to the wind-induced Ekman flow. The total cross-front Ekman transport, and thus the Ekman buoyancy flux ($B_E = \tau_x \partial_y b / \rho_0 f$), is essentially independent of the choice of BLT parameterizations. However, the destratification rate due to the Ekman flow does depend on the vertical shear. This effect will be quantified in Section 5.4.

Apart from that, the different vertical shear may also influence the evolution of symmetrical instability (SI) (e.g., Taylor and Ferrari, 2010). While SI

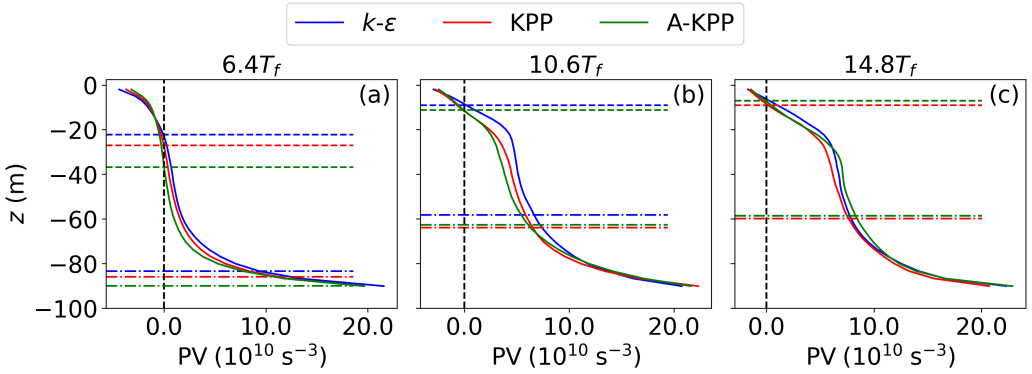

Figure 8: Vertical profiles of the frontal averaged potential vorticity (PV) at (a) $t = 6.4T_f$, (b) $t = 10.6T_f$, and (c) $t = 14.8T_f$. Dashed lines denote the bottom of the layer with negative PV. Dash-dotted lines denote the horizontal-averaged mixed layer depth in the frontal region. In panel (c), the blue dashed and dash-dotted lines overlap with the green lines.

is surely not resolved (at best partially-resolved) in the simulations described here (Bachman and Taylor, 2014; Mukherjee et al., 2016), it may be useful to examine the effects of BLT parameterizations on generating SI favorable conditions. Fig. 8 compares the frontal averaged potential vorticity (PV) in three time instances between cases with different BLT parameterizations. The PV is defined as

$$\mathrm{PV} = (f\mathbf{k} + \nabla \times \mathbf{u}) \cdot \nabla b, \tag{18}$$

where $\mathbf{k}$ is a unit vector in the vertical direction. Negative values of PV (opposite sign of f) indicate favorable conditions for SI. In the frontal region where the geostrophic shear is in thermal wind balance with the horizontal buoyancy gradient and the stratification is weak in the mixed layer, PV is negative. PV is further decreased by the along-front wind (Thomas, 2005) before the emergence of MLEs.

During this period, BLT modifies the magnitude of PV primarily through its effects on vertical mixing, altering the stratification and vertical shear and thereby modifying the slope of isopycnals at the front. As shown in Fig. 8, the ordering of the layer depth with negative PV is consistent with the ordering of the magnitude of turbulent vertical buoyancy flux shown in Fig. 6. The A-KPP case exhibits the strongest vertical buoyancy mixing, leading to weaker stratification and a deeper negative-PV layer, creating conditions that are more favorable for the development of SI. However, in the absence of active SI that would otherwise drive the PV toward zero, PV is increased by MLE-induced restratification in our simulations.

As shown in Fig. 8, when MLEs have just emerged at $t = 6.4T_f$, the A-KPP case exhibits a slightly deeper layer with negative PV, whereas the k-ε case shows the shallowest layer, with a depth difference of approximately 15 m. As the MLE-induced restratification progresses, the depth differences among the three cases decrease to less than 5 m at $t = 14.8T_f$. Throughout the evolution of MLEs, the k-ε case consistently shows a shallower layer with negative PV and a correspondingly shallower mixed layer compared to the KPP case. This behavior reflects the fact that, in our idealized model setup, MLE-induced restratification is the primary mechanism driving the shoaling of both the mixed layer and the layer with negative PV.

5.2. Secondary Circulation

In frontal regions, secondary circulation (SC) forms to flatten the isopycnals. The SC is important in modifying the frontogenesis process and also the available potential energy in the mixed layer (Sullivan and McWilliams, 2024). This section aims to analyze the impacts of BLT parameterization on

the SC. As MLEs dominate the flow when fully developed in the later stages, we focus our analysis of the SC on the early stages when BLT has a greater impact.

With steady down-front surface wind stress, the SC is affected by wind-driven Ekman flow, which can lead to a cross-front velocity v_{ek} even stronger than the SC itself. This cross-front velocity v_{ek} can be estimated from the balance between the Coriolis force and the divergence of BLT-induced momentum flux,

$$fv_{ek} = \partial_z \overline{w'u'}. \tag{19}$$

The SC-induced cross-front velocity v_{sc} can then be estimated from

$$v_{sc} = v - v_{ek}, \tag{20}$$

assuming that other contributions are negligible. Note that in the presence of inertial oscillations, v_{ek} is not always equal to the resolved submesoscale velocity v outside the front where $v_{sc} = 0$. However, this discrepancy can be greatly reduced by using the temporal average over an integer period, as shown in Fig. 9a.

Fig. 9b shows the cross-front velocity profiles within the frontal region. Solid lines represent the resolved submesoscale velocity, dashed lines represent the Ekman velocity calculated from (19), and dash-dotted lines denote the cross-front velocity due to SC according to (20). Only one inertial period is chosen for the temporal average because SC is not stable before $t = 3T_f$ and is soon strongly influenced by MLEs after $t = 5T_f$. As shown in Fig. 9b, a clockwise SC is formed in the frontal region, with similar magnitude of cross-front velocity at the top and bottom of the mixed layer. The differ-

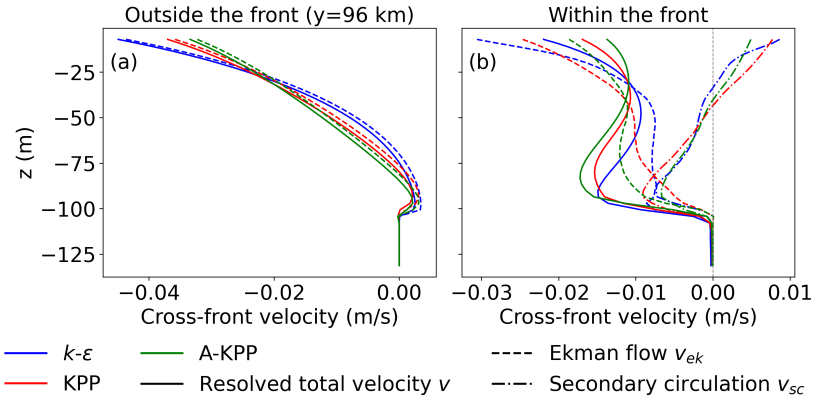

Figure 9: Vertical profiles of the cross-front velocities (a) outside the unstable front and (b) within the unstable front. Solid, dashed and dash-dotted lines denote the total cross-front velocity v, the component due to Ekman flow v_{ek}, and the component due to SC v_{sc}, respectively. All quantities are averaged along the front and over one inertial period (from $t = 3.3T_f$ to $t = 4.3T_f$). The quantities in (b) are further averaged in the frontal region defined in (12).

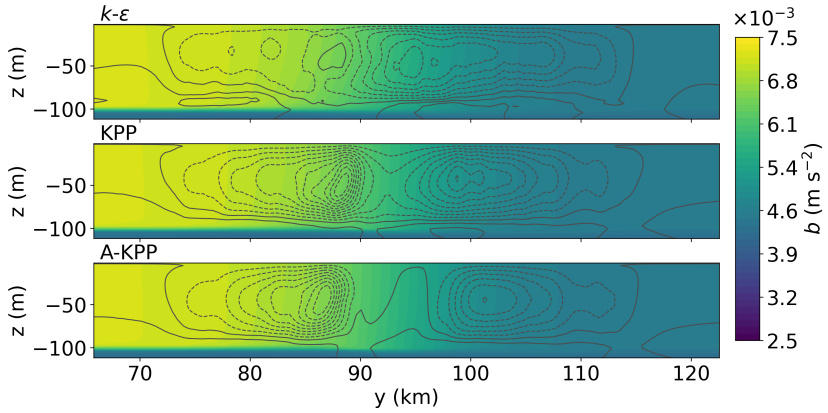

Figure 10: Stream function of the SC. Solid lines denote counterclockwise circulation while dashed lines represent clockwise circulation. The stream function is derived from the along-front and temporal ($3.3T_f \sim 4.3T_f$) mean of v_{sc}.

ences in SC caused by the three BLT parameterizations are smaller compared to the differences in the Ekman flow.

The stream function ψ_{sc} can be defined from v_{sc} to describe the SC

$$v_{sc} = \partial_z \psi_{sc}. \tag{21}$$

Fig.10 shows the stream function of SC during the same inertial period as in Fig.9. Although the cross-front velocities of the SC among the three cases with different BLT parameterizations are similar, the patterns of the stream function are different. The k-ε case shows a complete circulation across the front, which is slightly stronger on the cold side. However, the KPP and A-KPP cases show two separate circulations on two sides of the front, which are further encircled by a larger circulation across the front. This is consistent with the differences in the flow structure as indicated by the vertical vorticity in Fig. 3a–c.

5.3. Submesoscale Vertical Transport

Submesoscale frontogenesis and MLEs contribute significantly to the vertical transport of materials within the mixed layer and subduction into the thermocline. This section examines the impact of parameterized BLT on the submesoscale vertical transport.

Fig. 11 compares the vertical profiles of the frontal averaged submesoscale vertical velocity variance $\langle \widetilde{w^{\dagger 2}} \rangle_h$ in the three cases. The vertical velocity variance measures the magnitude of submesoscale vertical motions. In all cases, submesoscale vertical motions consistently reach their maximum magnitude in the middle of the mixed layer. Before the emergence of MLEs (Fig. 11a), the vertical motions are mainly induced by the flow convergence of frontogenesis. During this period, the profiles of $\langle \widetilde{w^{\dagger 2}} \rangle_h$ fluctuate over time, without a consistent ordering among the three cases. This is because the flow is effectively adjusting itself from thermal wind balance to TTW balance. In the early stage after the emergence of MLEs (Fig. 11b), the KPP and A-KPP cases exhibit intensified submesoscale vertical motions with maximum horizontally averaged values of $\langle \widetilde{w^{\dagger 2}} \rangle_h$ being 3.16×10^{-6} m^2 s^{-2} and 2.50×10^{-6} m^2 s^{-2}, respectively. The maximum value of $\langle \widetilde{w^{\dagger 2}} \rangle_h$ in the KPP case is about 1.44 times the maximum value in the k-ε case (2.20×10^{-6} m^2 s^{-2}). After MLEs are fully developed at $t = 10.1 T_f$ (Fig. 11c), the enhancement of vertical motions in the KPP and A-KPP cases persists, with maximum values of $\langle \widetilde{w^{\dagger 2}} \rangle_h$ reaching 2.01×10^{-6} m^2 s^{-2} and 2.24×10^{-6} m^2 s^{-2}. In contrast, the k-ε case shows smaller $\langle \widetilde{w^{\dagger 2}} \rangle_h$ (a maximum value of 1.61×10^{-6} m^2 s^{-2}). This suggests that the submesoscale vertical motions in these simulations are sensitive to the choice of BLT parameterizations.

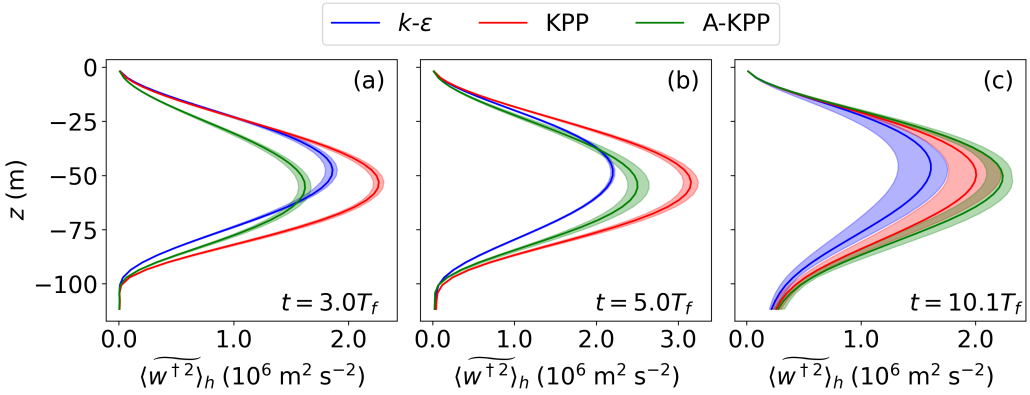

Figure 11: Vertical profiles of the submesoscale vertical velocity variance averaged over the frontal region in three time instances ($t = [3.0, 5.0, 10.1]T_f$). Colored shading denotes fluctuation among eight ensemble members.

Fig. 12 shows the evolution of the submesoscale vertical velocity variance $\langle\widetilde{w^{\dagger 2}}\rangle$ averaged in the frontal region in the three cases. After the emergence of MLEs at around $5T_f$, consistently stronger vertical motions are shown in the KPP case compared to the k-ε case. The maximum value of the frontally averaged vertical velocity variance in the KPP case is 1.92×10^{-6} m^2 s^{-2}, about 1.18 times that in the k-ε case (1.63×10^{-6} m^2 s^{-2}). This pattern of stronger submesoscale vertical motions in the KPP case is persistent until around $t = 15T_f$, when the submesoscale horizontal buoyancy gradient stops decreasing.

The frontal averaged and normalized vertical transport of horizontal momentum ($\langle\widetilde{w^{\dagger}u^{\dagger}}\rangle$ and $\langle\widetilde{w^{\dagger}v^{\dagger}}\rangle$) and the buoyancy ($\langle\widetilde{w^{\dagger}b^{\dagger}}\rangle$) due to MLEs are illustrated in Fig. 13. With different BLT parameterizations, the differences in the MLE-induced vertical transport of horizontal momentum are relatively small, particularly after the emergence of MLEs. The differences in the MLE-

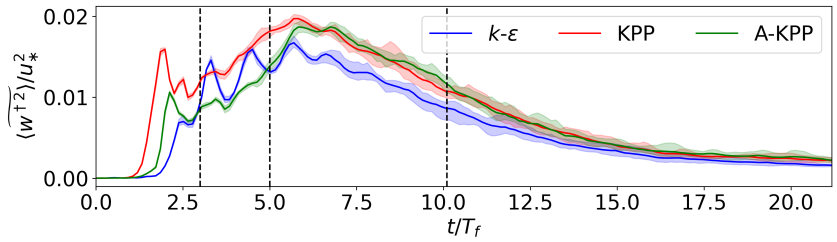

Figure 12: Time evolution of the submesoscale vertical velocity variance scaled by the friction velocity u_* and averaged over the frontal region. Colored shading represents fluctuation range among eight ensemble members. Dashed lines mark the three time instances shown in Fig. 11.

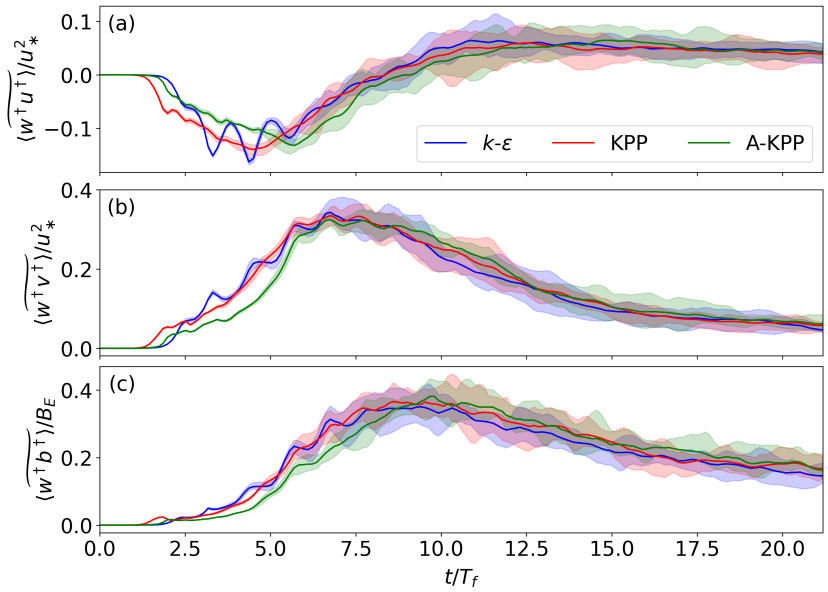

Figure 13: Same as Fig. 6, but for the vertical transport of horizontal momentum and buoyancy due to MLEs.

induced vertical buoyancy flux are also small, but exhibit some interesting patterns. In the early stage from $t = 5T_f$ to $t = 10T_f$, the A-KPP case shows slightly smaller $\langle\widetilde{w^\dagger b^\dagger}\rangle$ compared to both KPP and k-ε cases. But in the later stage after $t = 10T_f$, the ordering is changed to A-KPP > KPP > k-ε. The time evolution of the MLE-induced vertical buoyancy flux and the ordering among different BLT parameterizations are also similar to that of the BLT-induced vertical buoyancy flux (Fig. 6c) and submesoscale horizontal buoyancy gradient (Fig. 4e). However, these differences are mostly within the fluctuations between ensemble members, as shown by the colored shading. This indicates that variations in turbulent viscosity (and diffusivity) have a small impact on the MLE-induced vertical fluxes of momentum and buoyancy, especially once stratification ceases to increase.

5.4. Stratification

The evolution equation of the stratification can easily be derived by taking the vertical derivative of the buoyancy equation and is expressed as

$$\partial_t N^2 + \partial_z\partial_x(ub) + \partial_z\partial_y(vb) + \partial_z^2(wb) = -\partial_z^2\overline{w'b'}. \tag{22}$$

Here, interest is in the competing effects of MLE-induced restratification and BLT-induced destratification (parameterized) on the evolution of the along-front mean stratification. Therefore, the along-front average $\widetilde{(\cdot)}$ defined in Eq. (9) is performed, so that

$$\partial_t\widetilde{N^2} = -\left[\partial_z\partial_y(\widetilde{v}\widetilde{b}) + \partial_z^2(\widetilde{w}\widetilde{b})\right] - \left[\partial_z\partial_y\widetilde{v^\dagger b^\dagger} + \partial_z^2\widetilde{w^\dagger b^\dagger}\right] - \widetilde{\partial_z^2\overline{w'b'}}. \tag{23}$$

The terms in the first square bracket on the right-hand side represent the contributions of the submesoscale mean flow, while the terms in the second

square bracket denote the impact of submesoscale turbulence due to MLEs. The last term denotes the impact of BLT-induced vertical mixing. Note that the along-front average here is augmented by an ensemble average of all eight ensemble members to enhance the robustness of these statistics.

Fig. 14 shows vertical profiles of different terms in Eq. (23) averaged over the unstable frontal region (defined in a similar way as in Eq. (12)). It highlights distinct roles of submesoscale mean flow, submesoscale turbulence, and BLT-induced vertical mixing. The dominant contributors in the mean stratification budget are the vertical buoyancy flux induced by MLEs ($-\partial_z^2\widetilde{w^\dagger b^\dagger}$) and BLT ($-\partial_z^2\widetilde{\overline{w'b'}}$), showing restratification (positive) and destratification (negative) effects, respectively. The MLE-induced horizontal cross-front buoyancy flux ($-\partial_z\partial_y\widetilde{v^\dagger b^\dagger}$) has negligible effects. The impact of the submesoscale mean flow is also relatively small, exhibiting a weak destratification effect through Ekman buoyancy advection ($-\partial_z\partial_y(\widetilde{v}\widetilde{b})$) and a negligible effect from vertical buoyancy advection ($-\partial_z^2(\widetilde{w}\widetilde{b})$). This Ekman-induced destratification rate is ordered between different cases as k-ε > KPP > A-KPP. This ordering is consistent with the ordering of the cross-front vertical shear shown in Fig. 7. In particular, the weaker the cross-front vertical shear, the smaller the Ekman-induced destratification rate. This demonstrates the indirect effect of BLT-induced vertical mixing on the mean stratification by modifying the vertical structure of the Ekman flow.

As MLEs evolve, the BLT-induced destratification rate first increases ($t = 10.6T_f$ versus $t = 6.4T_f$) then gradually decreases ($t = 14.8T_f$ versus $t = 10.6T_f$) once stratification stabilizes (Fig. 4) in all three cases. This BLT-induced destratification is confined mainly in the upper 25 m or so, with

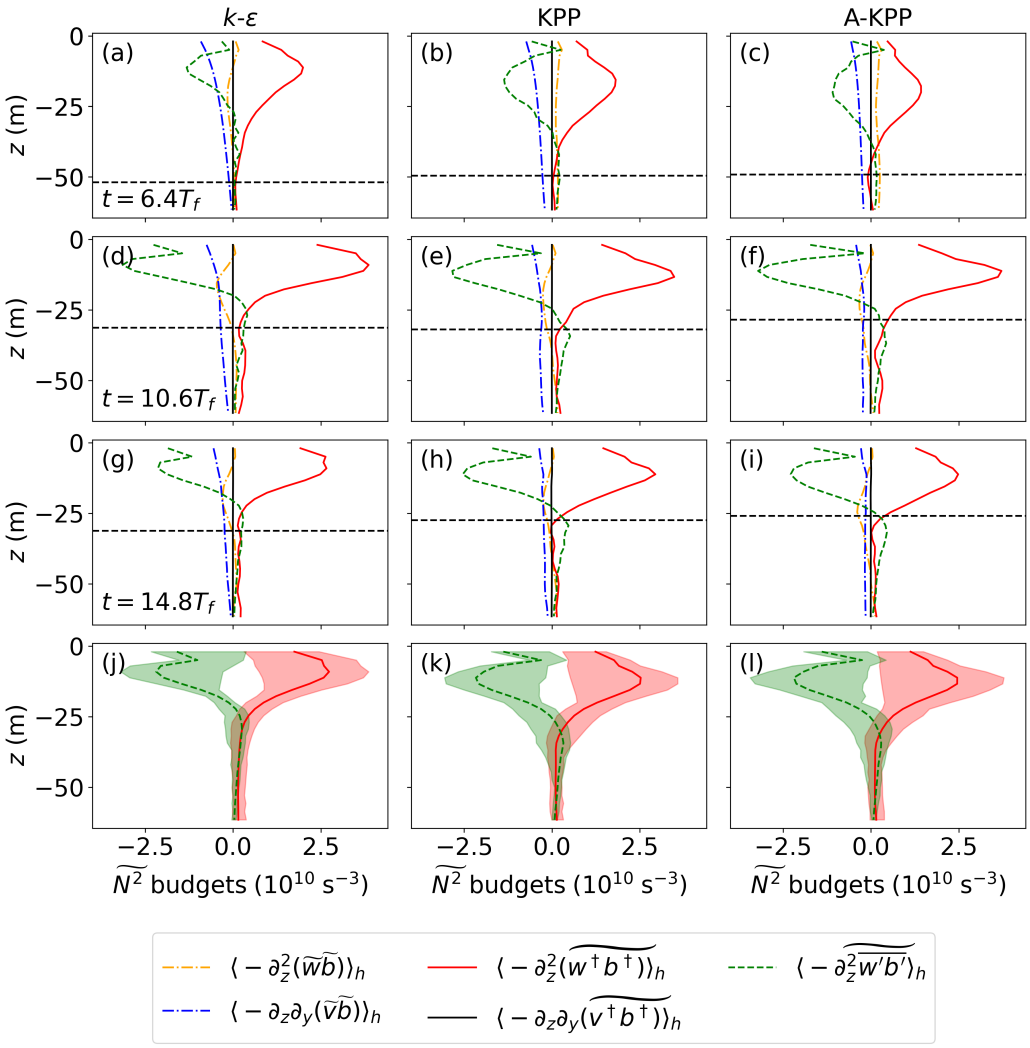

Figure 14: Vertical profiles of different terms in Eq. (23) in three time instances ($t = [6.4, 10.6, 14.8]T_f$, top three rows), as well as the temporal mean between $t = 5.0T_f$ and $t = 21.0T_f$ for the two dominant terms (last row). Colored shading represents the fluctuation range during this time period. Black dashed lines denote the mean boundary layer depth defined by the bulk Richardson number criterion as in KPP.

a maximum at a depth around $z = -10$ m. Different BLT parameterizations result in different BLT-induced destratification rates with substantial variation in time. In the early stage of MLE evolution (from $t = 5T_f$ to $t = 10T_f$), the A-KPP case shows a smaller BLT-induced destratification rate compared to the other two cases (k-$\varepsilon \sim$ KPP $>$ A-KPP at $t = 6.4T_f$). In addition, the maximum BLT-induced destratification rate occurs shallower in the k-ε case than the KPP and A-KPP cases. During the later stage (after $t = 10T_f$) when the mean stratification reaches a quasi-equilibrium (Fig. 4), the destratification rate in the k-ε case decreases more rapidly than in the other two cases (KPP $>$ A-KPP $\sim$ k-ε at $t = 14.8T_f$). The BLT-induced destratification rate is influenced not only by the magnitude of the turbulent viscosity and diffusivity but also by the state of the submesoscale flow. For example, larger turbulent viscosity (and diffusivity) may lead to more vertically homogenized submesoscale flow and buoyancy distribution, which may contribute to a smaller BLT-induced destratification rate. This dependence of the BLT-induced destratification rate on the evolution of MLEs may be stronger when the direct feedback from MLEs to BLT is considered (Johnson and Fox-Kemper, 2024).

Interestingly, there seems to be a good correlation between the BLT-induced destratification and MLE-induced restratification in these simulations. In other words, the MLE-induced restratification rate is consistently larger (or smaller) when the BLT-induced destratification rate is larger (or smaller), as is evident both in different time instances in a particular case and across different cases. For example, the MLE-induced restratification rate also increases in the early stage ($t = 10.6T_f$ versus $t = 6.4T_f$) and then

decreases in the later stage ($t = 14.8T_f$ versus $t = 10.6T_f$) as MLEs evolve. In addition, MLE-induced restratification in the case of k-ε is largest among the three cases at $t = 6.4T_f$ and $t = 10.6T_f$, but decreases rapidly afterwards, giving its position to KPP at $t = 14.8T_f$. All these patterns are consistent with the BLT-induced destratification rate. Such a strong correlation between the BLT-induced destratification and MLE-induced restratification is better illustrated in their temporal mean and fluctuations throughout the entire evolution period of MLEs (Fig. 14d,h,l). This suggests that parameterizations of BLT-induced destratification and MLE-induced restratification in a coarse resolution global ocean GCM, where both BLT and MLEs are unresolved, should probably be designed and implemented in tandem, rather than separately as is commonly done (e.g., Fox-Kemper et al., 2011; Li et al., 2016). This also aligns with the conclusions of Johnson and Fox-Kemper (2024).

The modification of MLE-induced restratification by parameterized BLT can be further illustrated by the spatial distribution of the restratification rate. Fig. 15 shows the averaged restratification rates along the front induced by MLEs and BLT at $t = 8.5T_f$, a time when stratification continues to increase. A comparison among the three cases reveals that the regions characterized by an enhanced rate of BLT-induced destratification are also regions with amplified MLE-induced restratification. Specifically, the BLT-induced destratification in the k-ε case shows broader regions with relatively higher magnitude compared to the other two cases, which is consistent with the patterns of the MLE-induced restratification. Moreover, as indicated by the black solid contours in Fig. 15, regions where the BLT-induced destrat-

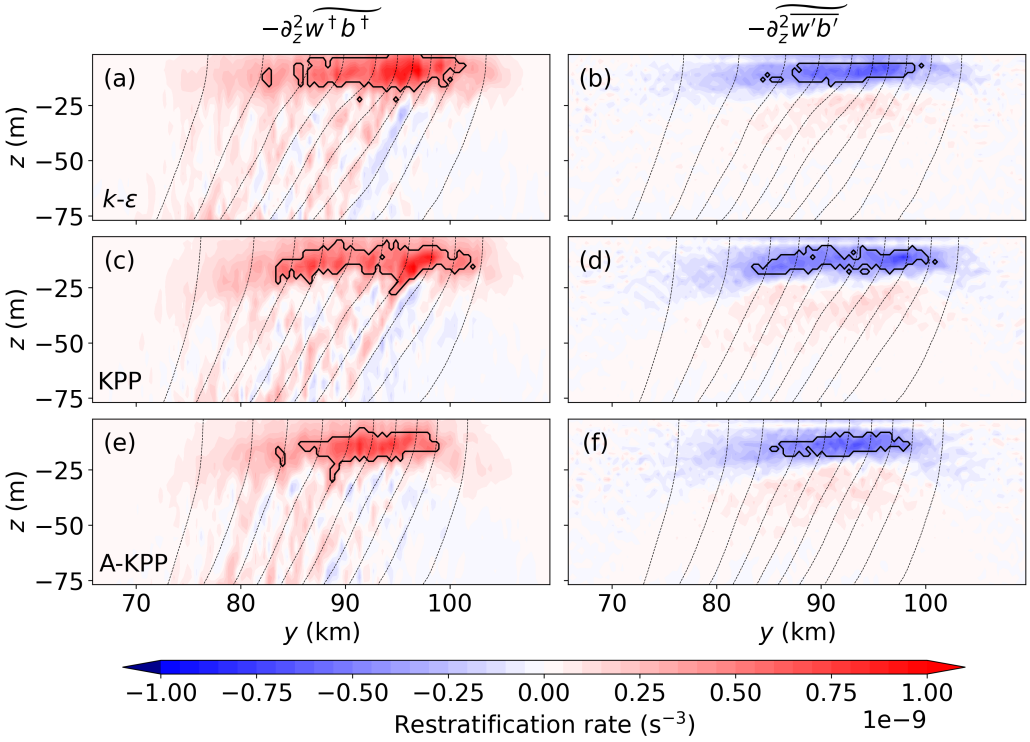

Figure 15: Along-front averaged restratification rate induced by MLEs (left panels) and BLT (right panels) in the three cases at $t = 8.5T_f$ when the stratification is increasing rapidly. Black dashed lines are isopycnals with an interval of 0.025 kg m^{-3}. Black solid contours enclose regions where the restratification rate is greater than 4×10^{-10} s^{-3} (left column) or smaller than -4×10^{-10} s^{-3} (right column).

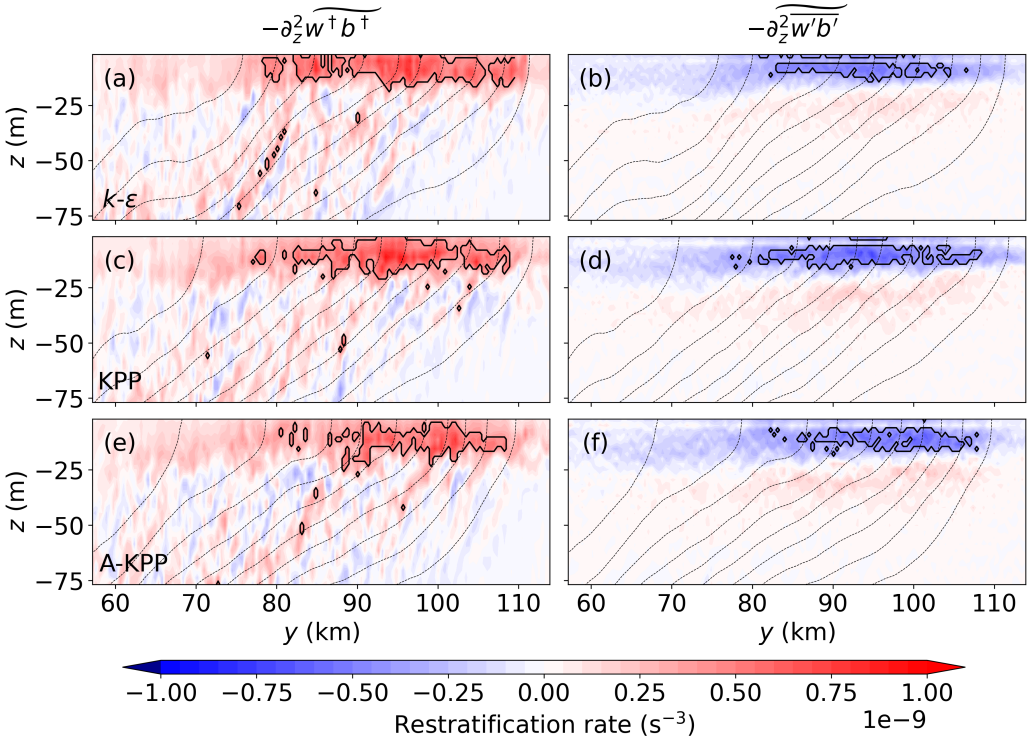

Figure 16: Same as Fig. 15, but at $t = 14.8T_f$. Black dashed lines are isopycnals with an interval of 0.022 kg m^{-3}.

ification rate exceeds 4×10^{-10} s^{-3} are also roughly the regions with MLE-induced restratification rates greater than 4×10^{-10} s^{-3}. Since the regions with strong MLE-induced restratification occupy a slightly larger spatial extent than the BLT-induced destratification, there is an overall increase in stratification in this stage (Fig. 4a). Similar compensating patterns can also be found when the MLEs are fully developed and the mean stratification reached a quasi-equilibrium at $t = 14.8T_f$ (Fig. 16).

The relationship between the BLT-induced destratification rate and the MLE-induced restratification rate aligns with the results of submesoscale vertical buoyancy transport in Section 5.3. In the presence of down-front surface wind forcing, the wind-driven BLT leads to the destratification of the mixed layer and tilts isopycnals towards vertical through turbulent vertical mixing of buoyancy. This process increases the potential energy at frontal region, which supplies energy for mixed layer instability that promotes submesoscale MLEs and the resulting restratification. This influence of parameterized BLT on MLEs occurs almost instantaneously in our simulations.

While we focus on a forcing regime in which the wind forcing and MLEs are comparable, we also run similar simulations under other forcing regimes with different surface wind stress and initial horizontal buoyancy gradient. A general conclusion from this practice is that submesoscale MLEs seem to be robust to surface wind stress. Even in cases with strong surface wind stress, when Ekman-induced destratification dominates, MLEs can still exist and grow at a similar rate. However, this growth rate is sensitive to lateral buoyancy variation, since available potential energy is required for the growth of MLEs. In cases with a weaker initial horizontal buoyancy gradi-

ent, it takes longer for the MLEs to develop fully. Thus, in conditions with weaker initial horizontal buoyancy gradient but stronger surface wind stress, the MLE-induced restratification may not be sufficiently strong to overcome the Ekman-induced destratification, forming a surface layer with negative stratification that is subject to gravitational instability. In these conditions, the correlation between the effects of MLEs and BLT on stratification is different from the relation reported here. However, once MLEs have been fully developed and MLE-induced restratification is sufficiently strong, the tight coupling between MLE-induced restratification and BLT-induced destratification can be clearly seen. A comprehensive exploration of the relative contribution of MLEs and BLT on stratification will likely require LESs on large horizontal domains that resolve both processes, which is left for future studies. Nevertheless, the results reported here may be helpful in guiding the choice of parameters in these computationally expensive LESs.

6. Conclusions

In this study, we examine the impact of parameterized BLT on the development and evolution of submesoscale MLEs in idealized double-front simulations under along-front surface wind forcing using MPAS-Ocean. Two popular BLT parameterizations (KPP and k-ε), as well as a simply modified version of KPP, are employed to demonstrate the impact of the BLT-induced vertical mixing on the vertical shear, vertical transport, and restratification induced by MLEs. The simulation configuration is chosen such that the effects of wind forcing and MLEs on the secondary overturning circulation are comparable.

Our results show that the evolution of MLEs can be divided into two distinct stages: a growth stage (approximately from $t = 5T_f$ to $t = 10T_f$), characterized by rapidly increasing kinetic energy and stratification; and a mature stage (approximately after $t = 10T_f$), when MLEs are fully developed and the kinetic energy and stratification in frontal regions plateau. The three different BLT parameterizations result in varying performances in vertical mixing during these two stages.

Throughout the evolution of MLEs, the total stratification, submesoscale kinetic energy and vertical vorticity, lateral buoyancy variation, and frontogenesis rate show limited sensitivity to the choice of BLT parameterizations, particularly when MLEs are fully developed with sizes exceeding 20 km. This insensitivity may be attributed to the dual roles of turbulent vertical mixing in submesoscale frontogenesis. Specifically, vertical mixing of momentum induces frontogenesis while vertical mixing of buoyancy inhibits it (Dauhajre et al., 2025). However, the magnitude of submesoscale vertical shear exhibits more pronounced differences among the three cases with different BLT parameterizations, primarily due to modifications in the turbulent momentum diffusion term in the TTW balance (McWilliams et al., 2015). In a more realistic configuration of submesoscale front or filament, where the upper ocean is influenced by diurnally varying atmospheric forcing as well as mesoscale strain, differences in the BLT parameterizations may have a more pronounced impact on the evolution of MLEs. In particular, variations in the simulated mixed layer depth with different BLT parameterizations may play a more important role than in the idealized configuration here. Exploring these effects in realistic configurations is left for future work.

In these idealized simulations, we show that submesoscale vertical motions, vertical buoyancy transports, and MLE-induced restratification rates are sensitive to turbulent vertical mixing, particularly with respect to buoyancy mixing. The ordering of the magnitude for vertical motions, buoyancy transports, and restratification rates is aligned closely with that of turbulent buoyancy flux. Furthermore, the vertical profiles of the MLE-induced restratification rates closely resemble those of the BLT-induced destratification rates (Fig. 14), with regions exhibiting higher BLT-induced destratification rates also showing intensified MLE-induced restratification rates (Fig. 15 and 16).

Additional sensitivity experiments are conducted to examine the robustness of our conclusions by varying different physical parameters, including the initial horizontal buoyancy gradients, the initial mixed layer depth, the magnitude and direction of wind stress, and the Coriolis parameter. The results suggest that the time required for MLEs to reach maturity varies substantially with these parameters, particularly with the initial horizontal buoyancy gradient. A stronger initial horizontal buoyancy gradient significantly accelerates the growth of MLEs. A robust feature across the sensitivity experiments is that the k-ε case consistently exhibits the smallest magnitude of the BLT-induced vertical fluxes of the along-front momentum and buoyancy, accompanied by the strongest vertical shear and the smallest vertical velocity variance in the unstable frontal region. However, the similarity between the vertical profiles of MLE-induced restratification and BLT-induced destratification (Fig. 14) does not always hold when the wind direction differs significantly. This is because the BLT-induced destratification rate is more sensitive to the local buoyancy gradient, whereas the angle between the Ek-

man transport and the horizontal buoyancy gradient can strongly modulate the Ekman-induced horizontal buoyancy advection. Despite these differences, a robust feature in all experiments is that the boundary layer consistently exhibits a substantially higher MLE-induced restratification rate when the BLT-induced destratification rate is higher. Moreover, regions with stronger MLE-induced restratification rates generally coincide with regions of intensified BLT-induced destratification rates, consistent with the coupled relationship between MLEs and BLT discussed in Section 5.4.

The tight coupling between MLEs and BLT in their contribution to vertical buoyancy transports and stratification rates may result from the modulation of available potential energy in frontal regions due to BLT-induced vertical mixing, which is extracted to promote MLEs through mixed layer instability. The vertical mixing of buoyancy steepens the isopycnals in the frontal region, thereby increasing the available potential energy. This process may enhance the efficiency of energy extraction by mixed layer instability, as evidenced by the larger submesoscale vertical buoyancy flux in cases with higher turbulent vertical buoyancy flux. Part of this potential energy is converted into submesoscale kinetic energy, promoting the growth of MLEs and resulting in restratification. This likely explains why regions with higher BLT-induced destratification rates also experience intensified MLE-induced restratification rates. This tight coupling between the two processes suggests that a quantitative assessment of the influence of submesoscale MLEs on vertical transport of heat and materials (e.g., Su et al., 2018) may need to consider the effect of parameterized BLT.

While we focus on the impact of parameterized BLT on simulated MLEs

in this study, these two processes are known to interact with each other (Hamlington et al., 2014; Sarkar et al., 2016; Skyllingstad et al., 2017; Sullivan and McWilliams, 2019). Parameterizations of one of them without considering the influences of the other often fail in frontal regions (Bodner et al., 2023; Johnson and Fox-Kemper, 2024). Recent work by Uchida et al. (2025) further demonstrated the sensitivity of the MLE parameterizations (e.g., Fox-Kemper et al., 2011; Bodner et al., 2023) to the choice of the BLT parameterizations. Together, these results suggest that future parameterizations may benefit from explicitly accounting for the joint effects of MLEs and BLT on vertical buoyancy fluxes, rather than treating the two processes separately. Our results support this perspective and point to the need for a more unified treatment of the interaction between MLEs and BLT to improve the representation of frontal stratification and vertical transport in ocean models.

Acknowledgment

This work is supported by a grant from the Research Grants Council of the Hong Kong Special Administrative Region, China (AoE/P-601/23-N), and the Guangdong Provincial Project (2023QN10H423). QL also acknowledges support from the Center for Ocean Research in Hong Kong and Macau (CORE), a joint research center between the Laoshan Laboratory and the Hong Kong University of Science and Technology (HKUST). MPAS-Ocean simulations presented in this work were performed using computational resources at the Earth and Environmental Systems Research Facility of the Hong Kong University of Science and Technology (Guangzhou).

References

Aparco-Lara, J., Torres, H.S., Gomez-Valdes, J., 2023. Impact of atmospheric cooling on the high-frequency submesoscale vertical heat flux. Journal of Geophysical Research: Oceans 128, e2023JC020029. doi:10.1029/2023JC020029.

Bachman, S.D., Taylor, J.R., 2014. Modelling of partially-resolved oceanic symmetric instability. Ocean Modelling 82, 15–27. doi:10.1016/j.ocemod.2014.07.006.

Boccaletti, G., Ferrari, R., Fox-Kemper, B., 2007. Mixed Layer Instabilities and Restratification. Journal of Physical Oceanography 37, 2228–2250. doi:10.1175/JPO3101.1.

Bodner, A.S., Fox-Kemper, B., Johnson, L., Van Roekel, L.P., McWilliams, J.C., Sullivan, P.P., Hall, P.S., Dong, J., 2023. Modifying the mixed layer eddy parameterization to include frontogenesis arrest by boundary layer turbulence. Journal of Physical Oceanography 53, 323–339. doi:10.1175/JPO-D-21-0297.1.

Callies, J., Ferrari, R., 2018. Baroclinic instability in the presence of convection. Journal of Physical Oceanography 48, 45–60. doi:10.1175/JPO-D-17-0028.1.

Canuto, V.M., Howard, A., Cheng, Y., Dubovikov, M.S., 2001. Ocean turbulence. Part I: One-point closure model-momentum and heat vertical diffusivities. Journal of Physical Oceanography 31, 1413–1426. doi:10.1175/1520-0485(2001)031<1413:OTPIOP>2.0.CO;2.

Capet, X., McWilliams, J.C., Molemaker, M.J., Shchepetkin, A.F., 2008a. Mesoscale to submesoscale transition in the California current system. Part I: Flow structure, eddy flux, and observational tests. Journal of Physical Oceanography 38, 29–43. doi:10.1175/2007JPO3671.1.

Capet, X., McWilliams, J.C., Molemaker, M.J., Shchepetkin, A.F., 2008b. Mesoscale to submesoscale transition in the California current system. Part II: Frontal processes. Journal of Physical Oceanography 38, 44–64. doi:10.1175/2007JPO3672.1.

Capet, X., McWilliams, J.C., Molemaker, M.J., Shchepetkin, A.F., 2008c. Mesoscale to submesoscale transition in the California current system. Part III: Energy balance and flux. Journal of Physical Oceanography 38, 2256–2269. doi:10.1175/2008JPO3810.1.

D'Asaro, E.A., 2014. Turbulence in the upper-ocean mixed layer. Annual Review of Marine Science 6, 101–15. doi:10.1146/annurev-marine-010213-135138.

Dauhajre, D.P., Srinivasan, K., Molemaker, M.J., Gula, J., Hypolite, D., McWilliams, J.C., Barkan, R., Young, W.R., 2025. Vertical mixing can both induce and inhibit submesoscale frontogenesis. Journal of Physical Oceanography 55, 1409–1433. doi:10.1175/JPO-D-24-0148.1.

de Boyer Montégut, C., Madec, C., Fischer, A.S., Lazar, A., Iudicone, D., 2004. Mixed layer depth over the global ocean: An examination of profile data and a profile-based climatology. Journal of Geophysical Research 109, C12003. doi:10.1029/2004JC002378.

Fox-Kemper, B., Bachman, S., Pearson, B., Reckinger, S., 2014. Principles and advances in subgrid modelling for eddy-rich simulations. CLIVAR Exchanges 19, 42–46.

Fox-Kemper, B., Danabasoglu, G., Ferrari, R., Griffies, S.M., Hallberg, R.W., Holland, M.M., Maltrud, M.E., Peacock, S., Samuels, B.L., 2011. Parameterization of mixed layer eddies. III: Implementation and impact in global ocean climate simulations. Ocean Modelling 39, 61–78. doi:10.1016/j.ocemod.2010.09.002.

Fox-Kemper, B., Ferrari, R., Hallberg, R., 2008. Parameterization of mixed layer eddies. Part I: Theory and diagnosis. Journal of Physical Oceanography 38, 1145–1165. doi:10.1175/2007JPO3792.1.

Golaz, J.C., Caldwell, P.M., Van Roekel, L.P., Petersen, M.R., Tang, Q., Wolfe, J.D., Abeshu, G., Anantharaj, V., Asay-Davis, X.S., Bader, D.C., Baldwin, S.A., Bisht, G., Bogenschutz, P.A., Branstetter, M., Brunke, M.A., Brus, S.R., Burrows, S.M., Cameron-Smith, P.J., Donahue, A.S., Deakin, M., Easter, R.C., Evans, K.J., Feng, Y., Flanner, M., Foucar, J.G., Fyke, J.G., Griffin, B.M., Hannay, C., Harrop, B.E., Hoffman, M.J., Hunke, E.C., Jacob, R.L., Jacobsen, D.W., Jeffery, N., Jones, P.W., Keen, N.D., Klein, S.A., Larson, V.E., Leung, L.R., Li, H.Y., Lin, W., Lipscomb, W.H., Ma, P.L., Mahajan, S., Maltrud, M.E., Mametjanov, A., McClean, J.L., McCoy, R.B., Neale, R.B., Price, S.F., Qian, Y., Rasch, P.J., Eyre, J.E.J.R., Riley, W.J., Ringler, T.D., Roberts, A.F., Roesler, E.L., Salinger, A.G., Shaheen, Z., Shi, X., Singh, B., Tang, J., Taylor, M.A., Thornton, P.E., Turner, A.K., Veneziani, M., Wan, H., Wang, H., Wang, S., Williams,

D.N., Wolfram, P.J., Worley, P.H., Xie, S., Yang, Y., Yoon, J.H., Zelinka, M.D., Zender, C.S., Zeng, X., Zhang, C., Zhang, K., Zhang, Y., Zheng, X., Zhou, T., Zhu, Q., 2019. The DOE E3SM coupled model version 1: Overview and evaluation at standard resolution. Journal of Advances in Modeling Earth Systems 11, 2089–2129. doi:10.1029/2018MS001603.

Griffies, S.M., Levy, M., Adcroft, A.J., Danabasoglu, G., Hallberg, R.W., Jacobsen, D., Large, W., Ringler, T., 2015. Theory and numerics of the Community Ocean Vertical Mixing (CVMix) project. URL: https://github.com/CVMix/CVMix-description/releases/tag/v0.93.

Hamlington, P.E., Van Roekel, L.P., Fox-Kemper, B., Julien, K., Chini, G.P., 2014. Langmuir–submesoscale interactions: Descriptive analysis of multiscale frontal spindown simulations. Journal of Physical Oceanography 44, 2249–2272. doi:10.1175/JPO-D-13-0139.1.

Hypolite, D., Romero, L., McWilliams, J.C., Dauhajre, D.P., 2023. Langmuir circulations transfer kinetic energy from submesoscales and larger scales to dissipative scales. Journal of Physical Oceanography 53, 253–268. doi:10.1175/JPO-D-22-0126.1.

Jiang, X., Li, Q., 2026. Archived source code for "Impact of parameterized wind-driven boundary layer turbulence on the development and evolution of submesoscale mixed layer eddies in an idealized front". URL: https://doi.org/10.5281/zenodo.18599450, doi:10.5281/zenodo.18599450.

965 Johnson, L., Fox-Kemper, B., 2024. Modification of boundary layer turbu-
966 lence by submesoscale flows. Flow 4, E20. doi:10.1017/flo.2024.17.

967 Large, W.G., Mcwilliams, J.C., Doney, S.C., 1994. Oceanic vertical mixing:
968 A review and a model with a nonlocal boundary layer parameterization.
969 Reviews of Geophysics 32, 363–403. doi:10.1029/94RG01872.

970 Li, Q., Reichl, B.G., Fox-Kemper, B., Adcroft, A., Belcher, S., Danaba-
971 soglu, G., Grant, A., Griffies, S.M., Hallberg, R.W., Hara, T., Har-
972 court, R., Kukulka, T., Large, W.G., McWilliams, J.C., Pearson, B.,
973 Sullivan, P., Van Roekel, L., Wang, P., Zheng, Z., 2019. Comparing
974 ocean surface boundary vertical mixing schemes including Langmuir tur-
975 bulence. Journal of Advances in Modeling Earth Systems 11, 3545–3592.
976 doi:10.1029/2019MS001810.

977 Li, Q., Van Roekel, L., 2021. Towards multiscale modeling of ocean surface
978 turbulent mixing using coupled MPAS-Ocean v6.3 and PALM v5.0. Geosci-
979 entific Model Development 14, 2011–2028. doi:10.5194/gmd-14-2011-2021.

980 Li, Q., Webb, A., Fox-Kemper, B., Craig, A., Danabasoglu, G., Large,
981 W.G., Vertenstein, M., 2016. Langmuir mixing effects on global cli-
982 mate: WAVEWATCH III in CESM. Ocean Modelling 103, 145–160.
983 doi:10.1016/j.ocemod.2015.07.020.

984 Mahadevan, A., 2016. The impact of submesoscale physics on primary
985 productivity of plankton. Annual Review of Marine Science 8, 161–184.
986 doi:10.1146/annurev-marine-010814-015912.

Mahadevan, A., D'Asaro, E., Lee, C., Perry, M.J., 2012. Eddy-Driven Stratification Initiates North Atlantic Spring Phytoplankton Blooms. Science 337, 54–58. doi:10.1126/science.1218740.

Mahadevan, A., Tandon, A., Ferrari, R., 2010. Rapid changes in mixed layer stratification driven by submesoscale instabilities and winds. Journal of Geophysical Research: Oceans 115. doi:10.1029/2008JC005203.

McWilliams, J.C., 2016. Submesoscale currents in the ocean. Proceedings of the Royal Society A: Mathematical, Physical and Engineering Science 472, 20160117. doi:10.1098/rspa.2016.0117.

McWilliams, J.C., Gula, J., Molemaker, M.J., Renault, L., Shchepetkin, A.F., 2015. Filament frontogenesis by boundary layer turbulence. Journal of Physical Oceanography 45, 1988–2005. doi:10.1175/JPO-D-14-0211.1.

McWilliams, J.C., Sullivan, P.P., 2000. Vertical mixing by Langmuir circulations. Spill Science and Technology Bulletin 6, 225–237. doi:10.1016/S1353-2561(01)00041-X.

Mukherjee, S., Ramachandran, S., Tandon, A., Mahadevan, A., 2016. Production and destruction of eddy kinetic energy in forced submesoscale eddy-resolving simulations. Ocean Modelling 105, 44–59. doi:10.1016/j.ocemod.2016.07.002.

Ramachandran, S., Tandon, A., Mahadevan, A., 2013. Effect of subgrid-scale mixing on the evolution of forced submesoscale instabilities. Ocean Modelling 66, 45–63. doi:10.1016/j.ocemod.2013.03.001.

1009 Reichl, B.G., Adcroft, A., Griffies, S.M., Hallberg, R., 2022. A Potential
1010 Energy Analysis of Ocean Surface Mixed Layers. Journal of Geophysical
1011 Research: Oceans 127, e2021JC018140. doi:10.1029/2021JC018140.

1012 Ringler, T., Petersen, M., Higdon, R.L., Jacobsen, D., Jones, P.W., Maltrud,
1013 M., 2013. A multi-resolution approach to global ocean modeling. Ocean
1014 Modelling 69, 211–232. doi:10.1016/j.ocemod.2013.04.010.

1015 Ringler, T.D., Thuburn, J., Klemp, J.B., Skamarock, W.C., 2010. A uni-
1016 fied approach to energy conservation and potential vorticity dynamics
1017 for arbitrarily-structured C-grids. Journal of Computational Physics 229,
1018 3065–3090. doi:10.1016/j.jcp.2009.12.007.

1019 Rocha, C.B., Gille, S.T., Chereskin, T.K., Menemenlis, D., 2016. Season-
1020 ality of submesoscale dynamics in the Kuroshio Extension. Geophysical
1021 Research Letters 43, 11,304–11,311. doi:10.1002/2016GL071349.

1022 Rodi, W., 1987. Examples of calculation methods for flow and mixing in
1023 stratified fluids. Journal of Geophysical Research: Oceans 92, 5305–5328.
1024 doi:10.1029/JC092iC05p05305.

1025 Sarkar, S., Pham, H., Ramachandran, S., Nash, J., Tandon, A., Buckley, J.,
1026 Lotliker, A., Omand, M., 2016. The interplay between submesoscale insta-
1027 bilities and turbulence in the surface layer of the Bay of Bengal. Oceanog-
1028 raphy 29, 146–157. doi:10.5670/oceanog.2016.47.

1029 Skyllingstad, E.D., Duncombe, J., Samelson, R.M., 2017. Baroclinic frontal
1030 instabilities and turbulent mixing in the surface boundary layer. Part II:

Forced simulations. Journal of Physical Oceanography 47, 2429–2454. doi:10.1175/JPO-D-16-0179.1.

Stone, P.H., 1966. On Non-Geostrophic Baroclinic Stability. Journal of the Atmospheric Sciences 23, 390–400. doi:10.1175/1520-0469(1966)023<0390:ONGBS>2.0.CO;2.

Stone, P.H., 1970. On Non-Geostrophic Baroclinic Stability: Part II. Journal of the Atmospheric Sciences 27, 721–726. doi:10.1175/1520-0469(1970)027<0721:ONGBSP>2.0.CO;2.

Su, Z., Wang, J., Klein, P., Thompson, A.F., Menemenlis, D., 2018. Ocean submesoscales as a key component of the global heat budget. Nature Communications 9, 775. doi:10.1038/s41467-018-02983-w.

Sullivan, P.P., McWilliams, J.C., 2019. Langmuir turbulence and filament frontogenesis in the oceanic surface boundary layer. Journal of Fluid Mechanics 879, 512–553. doi:10.1017/jfm.2019.655.

Sullivan, P.P., McWilliams, J.C., 2024. Oceanic frontal turbulence. Journal of Physical Oceanography 54, 333–358. doi:10.1175/JPO-D-23-0033.1.

Suzuki, N., Fox-Kemper, B., Hamlington, P.E., Van Roekel, L.P., 2016. Surface waves affect frontogenesis. Journal of Geophysical Research: Oceans 121, 3597–3624. doi:10.1002/2015JC011563.

Taylor, J.R., Ferrari, R., 2010. Buoyancy and wind-driven convection at mixed layer density fronts. Journal of Physical Oceanography 40, 1222–1242. doi:10.1175/2010JPO4365.1.

1053 Taylor, J.R., Ferrari, R., 2011. Shutdown of turbulent convection as a new
1054 criterion for the onset of spring phytoplankton blooms. Limnology and
1055 Oceanography 56, 2293–2307. doi:10.4319/lo.2011.56.6.2293.

1056 Taylor, J.R., Thompson, A.F., 2023. Submesoscale dynamics in the
1057 upper ocean. Annual Review of Fluid Mechanics 55, 103–127.
1058 doi:10.1146/annurev-fluid-031422-095147.

1059 Thomas, L.N., 2005. Destruction of potential vorticity by winds. Journal of
1060 Physical Oceanography 35, 2457–2466. doi:10.1175/JPO2830.1.

1061 Thomas, L.N., Lee, C.M., 2005. Intensification of ocean fronts by
1062 down-front winds. Journal of Physical Oceanography 35, 1086–1102.
1063 doi:10.1175/JPO2737.1.

1064 Uchida, T., Bodner, A.S., Reichl, B.G., Adcroft, A., Fox-Kemper, B., Ilicak,
1065 M., Bentsen, M., Marques, G.M., Large, W.G., 2025. Representation of
1066 surface mixed-layer eddies affects the large-scale ventilation of the global
1067 ocean. Authorea Preprints .

1068 Umlauf, L., Burchard, H., 2003. A generic length-scale equation for geo-
1069 physical turbulence models. Journal of Marine Research 61, 235–265.
1070 doi:10.1357/002224003322005087.

1071 Umlauf, L., Burchard, H., 2005. Second-order turbulence closure models for
1072 geophysical boundary layers. A review of recent work. Continental Shelf
1073 Research 25, 795–827. doi:10.1016/j.csr.2004.08.004.

1074 Van Roekel, L., Adcroft, A., Danabasoglu, G., Griffies, S.M., Kauff-
1075 man, B., Large, W., Levy, M., Reichl, B.G., Ringler, T., Schmidt, M.,

2018. The KPP boundary layer scheme for the ocean: Revisiting its formulation and benchmarking one-dimensional simulations relative to LES. Journal of Advances in Modeling Earth Systems 10, 2647–2685. doi:10.1029/2018MS001336.

Verma, V., Pham, H.T., Sarkar, S., 2022. Interaction between upper-ocean submesoscale currents and convective turbulence. Journal of Physical Oceanography 52, 437–458. doi:10.1175/JPO-D-21-0148.1.

Wang, Y., Dong, J., Ji, C., Dong, C., 2022. Dependence of submesoscale simulation on turbulence closure schemes in the Regional Ocean Modeling System (ROMS). Ocean Modelling 180, 102120. doi:10.1016/j.ocemod.2022.102120.

Yuan, J., Liang, J.H., 2021. Wind- and wave-driven ocean surface boundary layer in a frontal zone: Roles of submesoscale eddies and Ekman–Stokes transport. Journal of Physical Oceanography 51, 2655–2680. doi:10.1175/JPO-D-20-0270.1.